Nonlinear simulation of the effect of microenvironment on tumor growth

Macklin, Paul; Lowengrub, John

Published in:
Journal of Theoretical Biology

DOI:
10.1016/j.jtbi.2006.12.004

Publication date:
2007

Nonlinear simulation of the effect of microenvironment on tumor growth

Paul Macklin, John Lowengrub [1]

Department of Mathematics, 103 MSTB, University of California, Irvine, CA 92697, USA

Abstract

In this paper, we present and investigate a model for solid tumor growth that incorporates features of the tumor microenvironment. Using analysis and nonlinear numerical simulations, we explore the effects of the interaction between the genetic characteristics of the tumor and the tumor microenvironment on the resulting tumor progression and morphology. We find that the range of morphological responses can be placed in three categories that depend primarily upon the tumor microenvironment: tissue invasion via fragmentation due to a hypoxic microenvironment; fingering, invasive growth into nutrient-rich, biomechanically unresponsive tissue; and compact growth into nutrient-rich, biomechanically responsive tissue. We found that the qualitative behavior of the tumor morphologies was similar across a broad range of parameters that govern the tumor genetic characteristics. Our findings demonstrate the importance of the impact of microenvironment on tumor growth and morphology and have important implications for cancer therapy. In particular, if a treatment impairs nutrient transport in the external tissue (e.g., by anti-angiogenic therapy), increased tumor fragmentation may result, and therapy-induced changes to the biomechanical properties of the tumor or the microenvironment (e.g., anti-invasion therapy) may push the tumor in or out of the invasive fingering regime.

Key words: tumor microenvironment, nonlinear simulation, cancer therapy, morphological instability, tumor fragmentation, tumor growth, level set method, ghost fluid method, second-order accuracy, finite differences
1991 MSC: 65, 65MO6, 92C05

Email addresses: pmacklin@math.uci.edu (Paul Macklin), lowengrb@math.uci.edu (John Lowengrub).
URLs: http://math.uci.edu/∼pmacklin (Paul Macklin), http://math.uci.edu/∼lowengrb (John Lowengrub).
[1] Person to contact for paper.

1 Introduction

Cancer is a fundamental scientific and societal problem, and in the past few decades, vast resources have been expended in an effort to understand the root causes of cancer, to elucidate the intricacies of cancer progression, and to develop effective prevention and treatment strategies. In this paper, we present and investigate a model for solid tumor growth that incorporates features of the tumor microenvironment. Using analysis and nonlinear numerical simulations, we explore the effects of the interaction between the genetic characteristics of the tumor and the tumor microenvironment on the resulting tumor progression and morphology. Implications for cancer therapies are discussed.

Cancer is marked by several increasingly aggressive stages of development. The first stage, *carcinogenesis*, is believed to be characterized by a sequence of genetic mutations that promote growth (i.e., acquisition of oncogenes), circumvent apoptosis (i.e., inactivation or loss of tumor suppressor genes), or hinder DNA repair processes, thereby increasing the probability of acquiring oncogenes or inactivating tumor suppressor genes. (e.g. see Hanahan and Weinberg (2000) and Lehmann (2001).) In the second stage of development, *avascular growth* occurs as the cancer cells proliferate and form an *in situ* cancer. The local production of matrix-degrading enzymes and subsequent degradation of the extracellular matrix (ECM) may also play a role in providing room for the tumor to expand into the surrounding tissue. (See Hotary et al. (2003) and the discussion throughout Anderson (2005).) Since the tumor lacks a vasculature, nutrients (e.g., glucose and oxygen) are received only by diffusion through the surrounding tissue. As the tumor grows, less nutrient reaches the center of the tumor. Interior cells become hypoxic, begin to die (*necrose*), and are broken down by enzymes. As cell death in the tumor interior balances with cell proliferation on the boundary, a spherical tumor may reach a diffusion-limited size, usually on the order of 2-4 mm. However, if the tumor boundary acquires an irregular shape, additional nutrient becomes available to the tumor interior due to the increased surface area to volume ratio, and continued growth may result. Indeed, there are now a number of *in vitro* studies in which complex growth morphologies have been observed. (e.g. see Bredel-Geissler et al. (1992), Mueller-Kleiser (1997), Hedlund et al. (1999), Enmon Jr. et al. (2001), and Frieboes et al. (2006b).)

The next stage of tumor growth, *angiogenesis*, is characterized by the development of a tumor-induced neovasculature that grows from the main circulatory system toward the tumor in response to the imbalance of pro-angiogenic growth factors that are released by hypoxic cells in the tumor (e.g., vascular endothelial cell growth factor, or VEGF) relative to anti-angiogenic growth factors (e.g., angiostatin) present in the tumor microenvironment (Carmellet and Jain, 2000). In the final stage of tumor progression, *vascular growth*, the

tumor is supplied with nutrients from the newly-developed, although typically inefficient vasculature (Jain, 1990; Haroon et al., 1999; Hashizume et al., 2000). Additional mutations and epigenetic events may occur that lead to increased cellular motility and greater production of matrix degrading enzymes that degrade the ECM. This can lead to *invasion*, where either individual or collections of cancerous cells protrude and/or separate from the tumor and migrate through the surrounding tissue, or *metastasis*, where the invading tumor cells (or cell collections) enter the blood vasculature and/or lymphatic system and travel to distant locations.

The tumor microenvironment plays a crucial role in these processes. (e.g., see Hockel et al. (1996), Enam et al. (1998), Schmeichel et al. (1998), Sanson et al. (2002), and Pennacchietti et al. (2003).) For example, hypoxic microenvironments lead to the upregulation of HIF-1 target genes in both tumor cells and endothelial cells, including those responsible for the secretion of angiogenic growth factors and matrix degrading enzymes, metabolic changes such as increased glycolysis, and decreased cell-cell and cell-matrix adhesion (Kaur et al., 2005; Erler et al., 2006; Pouysségur et al., 2006). These conditions are associated with increased tumor invasiveness (Kaur et al., 2005; Erler et al., 2006; Pouysségur et al., 2006) and poor patient outcome (Hockel et al., 1996). However, the effects of the interaction between intra- and extratumoral processes on tumor progression and morphology are not well understood. Mathematical modeling has the potential to provide insight into these interactions though systematic studies of fundamental constituent processes.

Over the past ten years, the interest in the mathematical modeling and numerical simulation of cancer has increased dramatically. (See the reviews by Adam (1996), Bellomo et al. (2003), and Araujo and McElwain (2004a), Byrne et al. (2006), Sanga et al. (2006), and Quaranta et al. (2005).) A variety of modeling strategies is now available, each of which is well-suited to investigate one or more aspect of cancer. Cellular automata and agent-based modeling, where individual cells are simulated and updated based upon a set of biophysical rules, are particularly useful for studying carcinogenesis, natural selection, genetic instability, and interactions of individual cells with each other and the microenvironment. Because these methods are based on a series of rules for each cell, it is straightforward to translate biological processes (e.g., complex mutation pathways) into model rules. On the other hand, these models can be difficult to study analytically, and the computational cost increases rapidly with the number of cells modeled. Because a 1 mm tumor spheroid has over 500,000 cells, these methods can quickly become unwieldy when studying tumors of any significant size. For some examples of cellular automata modeling, see Anderson (2005), Alarcón et al. (2003), and Mallett and de Pillis (2006), and see Mansury et al. (2002) and Abbott et al. (2006) for examples of agent-based modeling.

In larger-scale systems where the cancer cell population is on the order of 1,000,000 or more, continuum methods provide a good modeling alternative. Early work (e.g. Greenspan (1976), Byrne and Chaplain (1996a), Byrne and Chaplain (1996b)) used ordinary differential equations (ODE) to model cancer as a homogeneous population, as well as partial differential equation (PDE) models restricted to spherical geometries. Linear and weakly nonlinear analyses have been performed to assess the stability of spherical tumors to asymmetric perturbations (e.g., Chaplain et al. (2001), Byrne and Matthews (2002), Cristini et al. (2003), and Li et al. (2006), and discussed in the reviews by Araujo and McElwain (2004a) and Byrne et al. (2006)) as a means to characterize the degree of aggression. Various interactions of the tumor with the microenvironment, such as stress-induced limitations of tumor growth, have also been studied in this context (e.g., Jones et al. (2000), Ambrosi and Mollica (2002, 2004), Roose et al. (2003), Araujo and McElwain (2004b, 2005), and Ambrosi and Guana (2006)). Most of the previous modeling has considered single-phase tumors. More recently, multiphase mixture models have been developed to provide a more detailed account of tumor heterogeneity. (e.g., see the work by Ambrosi and Preziosi (2002), Byrne and Preziosi (2003), and Chaplain et al. (2006).)

Very recently, nonlinear modeling has been performed to study the effects of shape instabilities on avascular, angiogenic, and vascular solid tumor growth. Cristini, Lowengrub, and Nie used boundary integral methods and performed the first fully nonlinear simulations of a continuum model of tumor growth in the avascular and vascularized growth stages with arbitrary boundaries (Cristini et al., 2003). This work investigated the nonlinear regime of shape instabilities and predicted the encapsulation of external, non-cancerous tissue by morphologically unstable tumors. Interestingly, shape instabilities were found to occur only in the diffusion-dominated, avascular regime of growth. The effect of the extratumoral microenvironment was not considered.

Zheng et al. (2005) extended this model to include angiogenesis and an extratumoral microenvironment by developing and coupling a new level set implementation with a hybrid continuous-discrete angiogenesis model originally developed by Anderson and Chaplain (1998). Zheng et al. investigated the nonlinear coupling between growth and angiogenesis. As in Cristini et al. (2003), it was found that low-nutrient (e.g. hypoxic) conditions may lead to instability. Zheng et al. did not fully investigate the interaction between the growth progression and the tumor microenvironment, but their work served as a building block for recent studies of the effect of chemotherapy on tumor growth by Sinek et al. (2004) and for studies of morphological instability and invasion by Cristini et al. (2005) and Frieboes et al. (2006b). Hogea et al. (2006) have also begun investigating tumor growth and angiogenesis using a level set method coupled with a continuous model of angiogenesis. In addition, Frieboes et al. (2006a) and Wise et al. (2006a,b) have recently developed a diffuse interface

implementation of solid tumor growth to study the evolution of multiple tumor cell species during progression.

In Macklin (2003) and Macklin and Lowengrub (2005, 2006), we also considered a level set-based extension of the tumor growth model that was previously investigated by Cristini et al. (2003) (described above). In these works, we developed new, highly-accurate numerical techniques to solve the resulting system of partial differential equations in a moving domain. These numerical methods are more accurate than those used by Zheng et al. (2005) and Hogea et al. (2006). Using these methods, we modeled tumor growth under a variety of conditions and investigated the role of necrosis in destabilizing the tumor morphology. We demonstrated that non-homogeneous nutrient diffusion inside the tumor leads to heterogeneous growth patterns that, when interacting with cell-cell adhesion, cause sustained morphological instability during tumor growth, as well as the repeated encapsulation of noncancerous tissue by the growing tumor.

In this paper, we extend the tumor growth models considered by Cristini, Lowengrub, Nie, Macklin, Zheng, and others (for example, Cristini et al. (2003), Macklin and Lowengrub (2005), and Zheng et al. (2005), all of which reformulated several classical models (Greenspan, 1976; McElwain and Morris, 1978; Adam, 1996; Byrne and Chaplain, 1996a,b; Chaplain, 2000)) to include more detailed effects of the microenvironment by allowing variability in nutrient availability and the response to proliferation-induced mechanical pressure (which models hydrostatic stress) in the tissue surrounding the tumor. In our model, the region surrounding the tumor aggregates the effects of ECM and noncancerous cells, which we characterize by two nondimensional parameters that govern the diffusional and biomechanical properties of the tissue. Fluids are assumed to move freely through the interstitium and ECM, and so such effects are currently neglected. The external nutrient and pressure variations, in turn, affect the evolution of the tumor in our model. Due to the computational cost of three-dimensional simulations, we shall focus our attention on two-dimensional tumor growth, although the model we develop applies equally well in three dimensions. In Cristini et al. (2003), it was found that the baseline model predicts similar morphological behavior for two-dimensional and three-dimensional tumor growth. This has been borne out by recent three-dimensional simulations by Li et al. (2006). We note that two-dimensional tumor growth may be well-suited to studying cancers that spread over large areas but are relatively thin, such as melanoma.

Using our model, we shall conduct a systematic investigation of the effect of the microenvironment on tumor growth over a broad range of biophysical parameters. In the process, we shall characterize the behavior predicted by the model and discuss the implications for cancer treatment. We note that by matching the results to known morphologies, one may infer the range of

validity of the model and obtain estimates of parameter values; we discuss this at the end of this paper. These simulations are difficult and require the development of accurate numerical techniques, which we present in this paper.

We find that the range of morphological responses can be placed in three categories that depend primarily upon the tumor microenvironment. In nutrient-poor microenvironments, tumors tend to break into small fragments and invade the surrounding tissue, regardless of the mechanical properties of the surrounding tissue. When placed in nutrient-rich tissue, the tumor morphology depends upon the biomechanical characteristics of the tissue. Tumors growing into mechanically unresponsive tissue develop buds that grow into long, invasive fingers. Tumors growing into softer, mechanically responsive tissue develop buds that do not grow, but rather connect with neighboring buds to capture external ECM. The overall morphology remains compact, with a large central abscess containing encapsulated ECM, fluid, and cellular debris similar to a necrotic core. We found that the qualitative behavior of the tumor morphologies was similar across a broad range of parameters that govern the tumor genetic characteristics. Our findings demonstrate the importance of the impact of microenvironment on tumor growth and morphology, and this has implications for cancer therapy: the impact of a therapy on the microenvironment may either positively or negatively impact the outcome of the treatment. A treatment that impairs nutrient delivery in the host tissue (e.g., using anti-angiogenic drugs) may increase tumor fragmentation, whereas a treatment that normalizies nutrient delivery may reduce or prevent tumor fragmentation. Therapies that affect the biomechanical responsiveness of the tumor or surrounding host tissue (e.g., anti-invasion therapy that alters cell-cell or cell-matrix adhesion) may either cause or prevent invasive fingering.

Using our model, we also investigate the internal structure of the tumors, including the volume fractions of the necrotic and viable portions of the tumor. We find that even during growth, the internal structure tends to stabilize due to apparent local equilibration of the tumors as characteristic feature sizes and shapes emerge. We also find that whereas the tumor morphology depends primarily upon the microenvironment, the internal structure is most strongly influenced by the genetic characteristics of the tumor, including resistence to necrosis, the rate at which the necrotic core is degraded, and the apoptosis rate. These results are not at all obvious from the examination of the model and underlying hypotheses alone. By hypothesis, the microenvironment, tumor genetics, and tumor morphology are all nonlinearly coupled. The tumor genetics determine biophysical properties like growth rates, which, in turn, are mediated by microenvironmental factors such as available nutrient supply. One would then expect that the tumor genetics have a greater impact on tumor morphology, and indeed, Cristini et al. (2003) found that the tumor genetics completely determine the morphological behavior when the microenvironment is not taken into account. While the important role of the microenvironment

is consistent with experiments in the literature, the observed dominance of the microenvironment in determining the morphology is intriguing. Likewise, the weak dependence of the internal tumor structure on the microenvironment and morphology is difficult to predict *a priori*. The model can be analyzed to make this prediction for tumor spheroids, but such an analysis ignores variation in tumor morphology and does not lead to obvious conclusions for the general case, where the morphology (and presumably volume) of the necrotic core depends upon the morphology of the tumor boundary.

We note that while our model captures the basic features of tumor growth, it does not currently incorporate the effects of elastic and residual stress, ECM degradation, signaling by promoters and inhibitors, angiogenesis, and competition between tumor subpopulations. These effects represent model refinements that can readily be added to our current modeling framework. We shall discuss our plans to address these and other refinements in the closing remarks in Section 5.

The contents of this paper are as follows: in Section 2, we describe the tumor growth and microenvironment models, nondimensionalize the resulting systems, and present an analysis of the internal structure of tumor spheroids that will be helpful in understanding non-spherical growth. In Section 3 and Appendix A, we give the important features of our level set/ghost fluid method and extend our technique to solve the Poisson-like equations on the full domain. In Section 3.2, we present a convergence study to demonstrate the accuracy of our technique. In Section 4, we present the results of a parameter study of tumor growth in a variety of microenvironments, categorize the characteristic tumor morphologies, investigate the causal link between microenvironment and tumor morphology, and analyze the link between the internal tumor structure and the tumor genetic parameters. In Section 5 and throughout the text, we discuss the clinical implications of the behavior predicted by our model. In Section 5, we also summarize our work, address known deficiencies in the model, and discuss ongoing modeling refinements.

2 Governing Equations

We study and extend a model for solid tumor growth that applies equally well in two and three dimensions (Cristini et al., 2003; Macklin, 2003; Macklin and Lowengrub, 2005; Zheng et al., 2005), which is a reformulation of several classical models (Greenspan, 1976; McElwain and Morris, 1978; Adam, 1996; Byrne and Chaplain, 1996a,b; Chaplain, 2000). We model an avascular tumor occupying a volume $\Omega(t)$ with boundary $\partial\Omega$, which we denote by Σ. The tumor is composed of a viable region Ω_V where nutrient (e.g., oxygen and glucose) levels are sufficient for tumor cell viability and a necrotic region Ω_N where

tumor cells die due to low nutrient levels and are broken down by enzymes. Note that $\Omega = \Omega_V \cup \Omega_N$.

The growing tumor also interacts with the surrounding microenvironment in the host tissue; we denote this region by Ω_H. The region Ω_H contains extracellular matrix (ECM) and a mixture of noncancerous cells, fluid, and cellular debris. As observed in Cristini et al. (2003), Macklin (2003), and Macklin and Lowengrub (2005), the growing tumor may encapsulate regions of Ω_H, and so these regions may lack living noncancerous cells. (See Figure A.1.) Hereafter, we shall refer to Ω_H as noncancerous tissue, although our model applies equally well to the case in which Ω_H contains only ECM, fluid, and cellular debris.

2.1 Nutrient Transport

We describe the net effect of nutrients and growth-promoting and inhibiting factors with a single nutrient c. In the viable region of the tumor Ω_V, the nutrient diffuses and is uptaken by proliferating cells. Letting $\widetilde{D} = \widetilde{D}(\mathbf{x}, t)$ denote the nutrient diffusivity, and defining λ_V to be the nutrient uptake rate by proliferating tumor cells, then the nutrient is governed by the reaction-diffusion equation

$$\frac{\partial c}{\partial t} = \nabla \cdot \left(\widetilde{D} \nabla c\right) - \lambda_V c, \qquad \mathbf{x} \in \Omega_V. \tag{1}$$

Taking λ_V to be constant, note that the total nutrient uptake $\lambda_V c$ decreases with c. This models the fall in metabolic and mitotic behavior (i.e., quiescence) as the tumor cells become hypoxic. In future work, we shall explicitly model the quiescent tumor cell population, as these cells are particularly important when considering the efficacy of therapy (Konopleva et al., 2002; Ravandi and Estrov, 2006).

In the necrotic region Ω_N, there is little or no nutrient uptake, as there are few proliferating cells. However, necrosing cells release their intracellular contents, which are both cytotoxic/growth-inhibiting (Freyer, 1988; Festjens et al., 2006) and oxygen-reactive (e.g., necrotic tissue rapidly reacts with reintroduced oxygen to form reactive oxygen species that react with and damage biological molecules (Kloner and Jennings, 2001; Galaris et al., 2006)). Recalling that the general nutrient c models the net effect of nutrients and growth-promoting and inhibiting factors, we can model these effects with a nutrient decay rate λ_D. Thus,

$$\frac{\partial c}{\partial t} = \nabla \cdot \left(\widetilde{D} \nabla c\right) - \lambda_D c, \qquad \mathbf{x} \in \Omega_N. \tag{2}$$

We assume that tumor cells uptake nutrient at a greater rate than noncancerous cells, and so nutrient uptake is negligible in Ω_H (Vaupel et al., 1989; Garber, 2004; Esteban and Maxwell, 2005; Ramanathan et al., 2005). Furthermore, we assume that there is little cellular debris in Ω_H and thereby no nutrient decay in that region. Therefore,

$$\frac{\partial c}{\partial t} = \nabla \cdot \left(\widetilde{D} \nabla c \right), \qquad \mathbf{x} \in \Omega_H. \tag{3}$$

Summarizing, the nutrient satisfies

$$\frac{\partial c}{\partial t} = \nabla \cdot \left(\widetilde{D} \nabla c \right) - \lambda(\mathbf{x}, t) c, \qquad \mathbf{x} \in \Omega \cup \Omega_H \tag{4}$$

where

$$\lambda(\mathbf{x}, t) = \begin{cases} 0 & \mathbf{x} \in \Omega_H \\ \lambda_V & \mathbf{x} \in \Omega_V \\ \lambda_D & \mathbf{x} \in \Omega_N. \end{cases} \tag{5}$$

Because nutrient diffusion, uptake, and decay all occur much more quickly than tumor growth, the quasi-steady assumption applies and $\partial c / \partial t \approx 0$.

The tumor cells become necrotic when the nutrient falls below a critical value c_N for cellular viability. Therefore, the viable and necrotic regions can be identified by the nutrient concentration:

$$\begin{aligned} \Omega_V &= \{ \mathbf{x} \in \Omega : c \geq c_N \} \\ \Omega_N &= \{ \mathbf{x} \in \Omega : c < c_N \}. \end{aligned} \tag{6}$$

By equation (6), the morphology and location of Ω_N depends upon c, i.e., $\Omega_N = \Omega_N(c)$. Because λ varies within the tumor based upon the position of the necrotic core $\Omega_N(c)$, we see that $\lambda = \lambda(\mathbf{x}, t, c)$, which makes the nutrient equation nonlinear. However, we can linearize the problem by setting $\lambda_D = \lambda_V$, i.e., $\lambda \equiv \lambda_V$ throughout the tumor. This modeling convenience allows us to solve for the nutrient concentration using linear solvers. In test simulations with nonlinear solvers that we are currently developing (not shown), we have found that this assumption does not significantly affect the qualitative features of the necrotic core morphology and the overall tumor progression.

We assume that the nutrient and nutrient flux are continuous across the tumor boundary Σ:

$$[c] = 0 \qquad \mathbf{x} \in \Sigma \tag{7}$$

$$\left[\widetilde{D}\nabla c \cdot \mathbf{n}\right] = 0 \qquad \mathbf{x} \in \Sigma, \tag{8}$$

where $\mathbf{n}$ is the outward unit normal vector.

Here, for any quantity $q(\mathbf{x})$ and any $\mathbf{x} \in \Sigma$, we define

$$\begin{aligned}[q(\mathbf{x})] &= q(\mathbf{x})\Big|_{\Omega} - q(\mathbf{x})\Big|_{\Omega_H} \\ &= \lim_{\Omega \ni \mathbf{y} \to \mathbf{x}} q(\mathbf{y}) - \lim_{\Omega_H \ni \mathbf{y} \to \mathbf{x}} q(\mathbf{y})\end{aligned} \tag{9}$$

to be the jump in q across the boundary Σ.

Nutrient delivery by the blood vasculature and uptake by noncancerous cells are assumed to be in balance outside of $\Omega \cup \Omega_H$. Therefore, we take

$$c \equiv c_\infty \qquad \mathbf{x} \in \partial(\Omega \cup \Omega_H) \tag{10}$$

on the far-field boundary.

In this paper, we shall consider the special case of avascular growth in piecewise homogeneous tissue and assume $\widetilde{D} \equiv D_H$ in Ω_H and $\widetilde{D} \equiv D_T$ in Ω, where D_H and D_T are (generally different) constants.

2.2 Cellular Velocity Field

The cells and ECM in the host tissue Ω_H and the viable tumor region Ω_V are affected by a variety of forces, each of which contributes to the cellular velocity field $\mathbf{u}$. The proliferating tumor cells in Ω_V generate an internal (oncotic) mechanical pressure (hydrostatic stress) that also exerts force on the surrounding noncancerous tissue in Ω_H. Tumor and noncancerous cells and the ECM can respond to pressure variations by overcoming cell-cell and cell-ECM adhesion and moving within the scaffolding of collagen and fibroblast cells (i.e., ECM) that provides structure to the host tissue. The ECM in Ω_H can deform in response to the pressure. Following previous work, we assume constant cell density and model cellular motion within the ECM as incompressible fluid flow in a porous medium. The response of the cells and the ECM to the pressure is governed by Darcy's law

$$\mathbf{u} = -\widetilde{\mu}\nabla P \qquad \mathbf{x} \in \Omega_V \cup \Omega_H, \tag{11}$$

where the cellular mobility $\widetilde{\mu} = \widetilde{\mu}(\mathbf{x})$ measures the overall ability of tissue to respond to the pressure. We note that $\widetilde{\mu}$ also measures the permeability of the

tissue to tumor cells. See Ambrosi and Preziosi (2002) and Byrne and Preziosi (2003) for further motivation of this approach from a mixture modeling point of view.

When tumor cells are in a state of hypoxia, cellular pathways that increase cell migration may become activated (Hockel et al., 1996; Kaur et al., 2005; Lester et al., 2005; Erler et al., 2006; Pouysségur et al., 2006). This may be modeled by increasing the mobility $\widetilde{\mu}$ as the nutrient level decreases or as a tactic response to nutrient gradients (Friedl and Wolf, 2003). In this paper, we shall focus upon the effects of proliferative pressure only; the effects of increased cellular motility in response to hypoxia will be considered in a future work (Anderson et al., 2006).

The outward normal velocity V of the tumor boundary Σ is given by

$$V = \mathbf{u} \cdot \mathbf{n} = -\widetilde{\mu} \nabla P \cdot \mathbf{n}, \tag{12}$$

where $\mathbf{n}$ is the outward unit normal vector along Σ. We assume that the normal velocity is continuous across the tumor boundary Σ, i.e., voids do not form between the tumor and host tissue.

2.3 Proliferation, Apoptosis, and Necrosis

In the viable region Ω_V, proliferation increases the number of tumor cells and thus the volume occupied by the viable region. Apoptosis decreases the total volume of Ω_V at a constant rate λ_A. We assume that cell birth and death are in balance in Ω_H, and so there is no change in the volume in that region. (Note that if there are no cells in Ω_H, then there is no cell birth or death, and the assumption still holds.) In fact, unvascularized tumors are often hypoxic, leading to glycolysis in the tumor and acidosis (a reduced pH level) in the surrounding healthy tissue (Gatenby and Gawlinski, 1996, 2003). Noncancerous cells cannot survive in this condition, leading to an imbalance in cell birth and death that results in a relative survival advantage for tumor cells and a potential volume loss in Ω_H when cells are present. This effect will be considered in a future work.

Putting this together as in Cristini et al. (2003), the change in volume is

$$\nabla \cdot \mathbf{u} = \begin{cases} 0 & \mathbf{x} \in \Omega_H \\ bc - \lambda_A & \mathbf{x} \in \Omega_V. \end{cases} \tag{13}$$

Here, b is a constant related to the tumor cell mitosis rate.

Throughout the necrotic core Ω_N, the enzymatic breakdown of necrotic tumor cells is assumed to decrease the tumor volume at a constant rate λ_N. This volume loss can be imposed via a nonlocal boundary condition on the boundary Σ_N of the necrotic core:

$$\begin{aligned}\int_{\Sigma_N} \mathbf{u}\cdot\mathbf{n}\, ds &= -\int_{\Sigma_N} \left(\tilde{\mu}\nabla P\cdot\mathbf{n}\right)\, ds \\ &= -\lambda_N \left|\Omega_N\right|, \end{aligned} \tag{14}$$

where $\mathbf{u}\cdot\mathbf{n}$ is the limit from inside Ω_V, and $|\Omega_N|$ denotes the area of Ω_N.

As a computational convenience, we can achieve the correct volume loss by continuously extending the velocity $\mathbf{u}$ into Ω_N. Instead of using (14), we define

$$\nabla\cdot\mathbf{u} = -\lambda_N, \qquad \mathbf{x}\in\Omega_N. \tag{15}$$

We assume that voids do not form between the viable and necrotic regions. Therefore, we choose our extension such that the normal velocity is continuous across the necrotic boundary, i.e.,$[\mathbf{u}\cdot\mathbf{n}] = 0$ across Σ_N. We note that because Σ_N is determined by the nutrient level, it is not a material boundary and is not advected by the velocity field $\mathbf{u}$; the extension of the velocity field is used solely to yield the correct volume change in the tumor necrotic core.

One way to attain this is to extend the pressure continuously into the necrotic core as well, by taking

$$\begin{aligned} \mathbf{u} &= -\tilde{\mu}\nabla P && \mathbf{x}\in\Omega_N \\ [P] &= 0 && \mathbf{x}\in\Sigma_N \\ [-\tilde{\mu}\nabla P\cdot\mathbf{n}] &= 0 && \mathbf{x}\in\Sigma_N. \end{aligned} \tag{16}$$

We note that the jump condition $[P] = 0$ across Σ_N models low cellular adhesion and is consistent with the increased cellular mobilty observed in hypoxic cells (Brizel et al., 1996; Cairns et al., 2001; Hoeckel and Vaupel, 2001; Postovit et al., 2002; Rofstad et al., 2002; Pouysségur et al., 2006). We close this section by noting that (16) automatically satisfies $[\mathbf{u}\cdot\mathbf{n}] = 0$ on Σ_N.

2.4 Mechanical Pressure

We can obtain an equation for the mechanical pressure in $\Omega \cup \Omega_H$ by combining (11) and (13) and by noting the pressure extension in (16):

$$-\nabla \cdot (\widetilde{\mu} \nabla P) = \begin{cases} 0 & \mathbf{x} \in \Omega_H \\ bc - \lambda_A & \mathbf{x} \in \Omega_V \\ -\lambda_N & \mathbf{x} \in \Omega_N. \end{cases} \tag{17}$$

By the continuity of the normal velocity across the tumor boundary, by Darcy's law (11) there is no jump in the normal derivative $\widetilde{\mu} \nabla P \cdot \mathbf{n}$ across Σ. Following Cristini et al. (2003) and others, we model cell-cell adhesion forces in the tumor by introducing a Laplace-Young surface tension boundary condition. Therefore,

$$[P] = \gamma \kappa \qquad \mathbf{x} \in \Sigma \tag{18}$$

$$0 = [\mathbf{u} \cdot \mathbf{n}] = -[\widetilde{\mu} \nabla P \cdot \mathbf{n}] \qquad \mathbf{x} \in \Sigma, \tag{19}$$

where κ is the mean curvature and γ is a constant cell-cell adhesion parameter.

Cellular proliferation and death are in balance outside of $\Omega \cup \Omega_H$. Therefore,

$$P \equiv P_\infty \qquad \mathbf{x} \in \partial(\Omega \cup \Omega_H). \tag{20}$$

on the far-field boundary.

In this paper, we shall consider the special case of avascular growth in piecewise homogeneous tissue and take $\widetilde{\mu} \equiv \mu_H$ in Ω_H and $\widetilde{\mu} \equiv \mu_T$ in Ω, where μ_H and μ_T are constants that are generally not equal. Note that because $\widetilde{\mu}$ is constant within the tumor (and across Σ_N), the pressure boundary conditions across Σ_N in (16) are automatically satisfied for any C^1 smooth solution P.

2.5 Nondimensionalization

Following Cristini et al. (2003), Macklin (2003), Macklin and Lowengrub (2005), and Zheng et al. (2005), we first note that the nutrient concentration equation reveals intrinsic diffusional length (L) and relaxation time (λ_R^{-1}) scales:

$$L = \sqrt{\frac{D_T}{\lambda_V}} \quad \text{and} \quad \lambda_R = \frac{\mu_T \gamma}{L^3}, \tag{21}$$

Note that $L \approx 200$ μm (Cristini et al., 2003; Macklin, 2003; Macklin and Lowengrub, 2005). We nondimensionalize the nutrient and pressure by

$$\sigma = \frac{c}{c_\infty} \quad \text{and} \quad p = \frac{L}{\gamma}(P - P_\infty). \tag{22}$$

As in Zheng et al. (2005), we define the dimensionless numbers

$$G = \frac{\lambda_M}{\lambda_R} = \frac{bc_\infty}{\lambda_R}, \quad G_N = \frac{\lambda_N}{\lambda_M}, \quad A = \frac{\lambda_A}{\lambda_M}, \quad \text{and} \quad N = \frac{c_N}{c_\infty}, \tag{23}$$

where $\lambda_M = bc_\infty$ gives an intrinsic mitosis rate. The nondimensional parameter G gives the mitosis rate relative to the rate of relaxation due to cell-cell adhesion in the tumor and is a measure of tumor aggressiveness. G_N and A measure the rates of enzymatic degradation of the necrotic core and apoptosis relative to the mitosis rate, respectively. N is the threshold nutrient level for cell viability.

Using these scales, the nondimensionalized nutrient concentration we solve for satisfies

$$\begin{cases} D\nabla^2\sigma = 0 & \mathbf{x} \in \Omega_H \\ \nabla^2\sigma = \sigma & \mathbf{x} \in \Omega \\ [\sigma] = 0 & \mathbf{x} \in \Sigma \\ D\nabla\sigma\Big|_\Omega \cdot \mathbf{n} = \nabla\sigma\Big|_{\Omega_H} \cdot \mathbf{n} & \mathbf{x} \in \Sigma \\ \sigma \equiv 1 & \mathbf{x} \in \partial(\Omega \cup \Omega_H). \end{cases} \tag{24}$$

Here, $D = D_H/D_T$ provides a measure of the nutrient richness of the tumor microenvironment relative to the tumor.

The nondimensionalized pressure solves

$$\begin{cases} \mu\nabla^2 p = 0 & \mathbf{x} \in \Omega_H \\ \nabla^2 p = \quad G(\sigma - A) & \mathbf{x} \in \Omega_V \\ \nabla^2 p = -GG_N & \mathbf{x} \in \Omega_N \\ [p] = \kappa & \mathbf{x} \in \Sigma \\ \mu\nabla p\Big|_\Omega \cdot \mathbf{n} = \nabla p\Big|_{\Omega_H} \cdot \mathbf{n} & \mathbf{x} \in \Sigma \\ p \equiv 0 & \mathbf{x} \in \partial(\Omega \cup \Omega_H). \end{cases} \tag{25}$$

Here, $\mu = \mu_H/\mu_T$ is a measure of the relative ability of the external tissue to (biomechanically) respond to the pressure, compared to the biomechanical response of the tumor. Using this definition of μ, the nondimensional normal velocity that we use to update the tumor boundary position is given by

$$V = -\mu \nabla p\big|_{\Omega_H} \cdot \mathbf{n} = -\nabla p\big|_{\Omega} \cdot \mathbf{n}. \tag{26}$$

In this paper, we model $\Omega \cup \Omega_H$ to be everything inside of the ball

$$B(\mathbf{x}_{\text{cent}}, R+1), \tag{27}$$

where

$$R = \sup\{|\mathbf{x} - \mathbf{x}_{\text{cent}}| : \mathbf{x} \in \Omega\} \tag{28}$$

is the largest distance from the center of mass $\mathbf{x}_{\text{cent}}$ of the tumor. Notice that this ball contains the tumor Ω and all noncancerous tissue that is within the diffusional distance from the tumor. See Figure A.1. Lastly, we note that the viable and necrotic regions of the tumor are given by

$$\Omega_V = \{\mathbf{x} \in \Omega : \sigma(\mathbf{x}) \geq N\} \tag{29}$$
$$\Omega_N = \{\mathbf{x} \in \Omega : \sigma(\mathbf{x}) < N\}. \tag{30}$$

2.6 Analysis of Volume Fractions for Tumor Spheroids

Following Byrne and Chaplain (1996a) and Cristini et al. (2003), we obtain and analyze the steady-state, two-dimensional circular solution of the full tumor system; the analysis for three-dimensional growth is similar. The results of the analysis will be instructive when we interpret our nonlinear simulation results for more complex geometries.

We shall solve for the exact nutrient concentration, pressure, and tumor boundary velocity. Using the exact tumor boundary velocity, we can find the equilibrium radii of the tumor (R_∞) and the necrotic core ($R_{N,\infty}$) and calculate the (two-dimensional) necrotic volume fraction:

$$\frac{\text{Volume}_{\text{necrotic}}}{\text{Volume}_{\text{tumor}}} = \left(\frac{R_{N,\infty}}{R_\infty}\right)^2. \tag{31}$$

We seek to understand the sensitivity of the necrotic volume fraction to D, μ, A, G, G_N, and N.

For simplicity of analysis, we first assume that $D \gg 1$ and examine the effects of D later in this section. If $R = R(t)$ is the radius of the tumor at time t, then $\sigma \approx 1$ in the region $R < r \leq R+1$, and the nutrient concentration $\sigma(r,t)$ is given by

$$\sigma(r,t) = \begin{cases} \frac{I_0(r)}{I_0(R)} & 0 \leq r \leq R \\ 1 & R < r \leq R+1, \end{cases} \tag{32}$$

where $I_0(x)$ is the 0^{th} modified Bessel function of the first kind.

Once the nutrient concentration profile is known, we can define

$$R_N(t) = \{r : \sigma(r) = N\} = I_0^{-1}\left(N\, I_0(R)\right) \tag{33}$$

to be the radius of the necrotic core at time t. Notice that R_N is completely determined by R and N.

The cellular velocity is given by

$$\mathbf{u} = -\begin{cases} p'(r)\,\mathbf{r} & 0 \leq r \leq R(t) \\ \mu p'(r)\,\mathbf{r} & R(t) < r \leq R(t)+1, \end{cases} \tag{34}$$

where $\mathbf{r}$ is the outward unit vector. By the continuity of the cellular velocity across $R(t)$, the velocity of the tumor boundary $R'(t)$ is

$$R'(t) = -\lim_{r \uparrow R(t)} p'(R(t)) = -\mu \lim_{r \downarrow R(t)} p'(R(t)). \tag{35}$$

When the tumor has reached its equilibrium radius R_∞,

$$0 = \lim_{r \uparrow R_\infty} p'(R_\infty) = \mu \lim_{r \downarrow R_\infty} p'(R_\infty). \tag{36}$$

Because $p(R_\infty + 1) = 0$, we see that $p \equiv 0$ on $R_\infty < r \leq R_\infty + 1$ when the tumor has reached its steady size, and

$$0 = \mu \lim_{r \downarrow R_\infty} p'(R_\infty). \tag{37}$$

Therefore, μ has no impact on the equilibrium radii R_∞ and $R_{N,\infty}$, and hence the equilibrium necrotic tumor volume fraction. For simplicity of analysis, we

shall now assume $\mu \gg 1$, in which case the exact solution of the pressure is

$$p(r) = \begin{cases} d_1 + \frac{1}{4} G G_N r^2 & 0 \le r \le R_N \\ d_2 + d_3 \ln r - G \frac{I_0(r)}{I_0(R)} + \frac{1}{4} A G r^2 & R_N < r \le R \\ 0 & R < r \le R + 1, \end{cases} \tag{38}$$

where d_1, d_2, and d_3 are chosen to satisfy the continuity and boundary conditions:

$$d_1 + \frac{1}{4} G G_N R_N^2 = d_3 + d_4 \ln R_N - G \frac{I_0(R_N)}{I_0(R)} + \frac{1}{4} A G R_N^2 \tag{39}$$

$$\frac{1}{2} G G_N R_N = \frac{d_4}{R_N} - G \frac{I_1(R_N)}{I_0(R)} + \frac{1}{2} A G R_N \tag{40}$$

$$d_3 + \ln R - G + \frac{1}{4} A G R^2 = \frac{1}{R}. \tag{41}$$

Notice that we can explicitly solve for d_4 and find the boundary velocity:

$$\begin{aligned} R'(t) &= -p'(R) \\ &= -G \left(\frac{1}{2} \frac{R_N^2}{R} (G_N - A) + \frac{I_1(R_N)}{R I_0(R)} - \frac{I_1(R)}{I_0(R)} + \frac{1}{2} A R \right). \end{aligned} \tag{42}$$

To find the equilibrium radius R_∞, we set (42) equal to zero. Notice that G scales out, and so R_∞ (and thereby the equilibrium necrotic volume fraction) depends only upon A, G_N, N, and $R_{N,\infty}$, which itself depends only upon R_∞ and N. Therefore, for large D, the necrotic volume fraction is a function of A, G_N, and N, and independent of G and μ. In fact, we have found that this trend holds for any fixed value of D, and the necrotic volume fraction is independent of D for values greater than approximately 10. For example, if $G = 20$, $G_N = 1$, $A = 0$, and $N = 0.35$, then the necrotic volume fraction increases rapidly from 26.4% ($D = 0.25$) to 35.8% ($D = 10$), increases more slowly to approximately 36.3% ($D = 20$), and then quickly approaches a limiting value of approximately 36.9% as D increases further.

By solving (32) and (42), one can examine the evolution of the necrotic volume fraction as a tumor spheroid approaches its equilibrium size. We have found that the relative rate of change of the necrotic volume fraction is approximately equal to the relative rate of change in the spheroid radius. (e.g., if the radius is increasing at 0.1% per time, then the necrotic volume fraction is increasing at a similar rate.) Thus, a steady necrotic volume fraction indicates that a tumor spheroid has reached a steady state.

As we shall verify numerically, it turns out that even during growth, the viable and necrotic volume fractions of nonspherical tumors tend toward constant values that depend primarily upon A, D, G_N, and N. This indicates the emergence of characteristic feature sizes within the tumor and suggests local equilibration. In large part, the emergent local configuration is determined by the thickness of the viable rim and the size of the necrotic core. The viable rim size is determined by how well nutrients penetrate the tumor (D), the amount of apoptosis (A), and the threshold nutrient level for necrosis (N). The size of the necrotic core is determined by how quickly necrotic tumor cells are broken down and removed (G_N). This is in contrast with the spherical tumor case, where the volume fractions only stabilize when the tumor reaches its (global) equilibrium radius.

We note that because a spheroid has minimum surface area to volume ratio, it provides a growing tumor with the least access to nutrient and therefore the largest necrotic volume fraction. Therefore, for non-spheroids, we expect smaller necrotic volume fractions. In fact, it is the attempt of growing tumors to improve access to nutrient that often drives morphological instability.

3 Numerical Method

We adapt and apply the numerical techniques we recently described in Macklin (2003) and Macklin and Lowengrub (2005, 2006). Because we anticipate frequent tumor morphology changes (e.g., the tumor breaks into fragments, or tumor fragments merge), we use the level set method: we introduce an auxiliary "level set" signed distance function φ satisfying $\varphi < 0$ inside Ω, $\varphi > 0$ outside Ω, and $\varphi = 0$ on the tumor boundary Σ. See Figure A.2. For more information on the level set method and its application to fluid mechanics, please see Osher and Sethian (1988), Sussman et al. (1994), Malladi et al. (1995, 1996), Adalsteinsson and Sethian (1999), Sethian (1999), Osher and Fedkiw (2001, 2002), and Sethian and Smereka (2003).

At every fixed simulation time, our method consists of the following steps:

(1) Solve for the nutrient with Equation (24). Note that this determines the updated position of the necrotic core boundary Σ_N.
(2) Solve for the pressure with Equation (25).
(3) Update the position of the boundary Σ by evolving the level set function φ with the normal velocity V in Equation (26).
(4) Maintain φ as a distance function.

3.1 Solution of the Tumor System

We solve for all quantities on a regular Cartesian mesh that is dynamically resized to contain the growing tumor Ω and the noncancerous tissue Ω_H. Both the nutrient and pressure equations take the form

$$\begin{aligned} \alpha \nabla^2 u = f_1(\mathbf{x},t) + f_2(\mathbf{x},t)u \quad & \text{in} \quad \Omega \text{ and } \Omega_H & (43)\\ [u] = g(\mathbf{x},t) \quad & \text{on} \quad \Sigma & (44)\\ [\alpha \nabla u \cdot \mathbf{n}] = 0 \quad & \text{on} \quad \Sigma & (45)\\ u \equiv u_O \quad & \text{on} \quad \partial(\Omega \cup \Omega_H) & (46) \end{aligned}$$

where u is either σ or p,

$$\alpha = \begin{cases} \alpha_T & \text{in} \quad \Omega \\ \alpha_H & \text{in} \quad \Omega_H, \end{cases} \tag{47}$$

and α_T and α_H are positive constants. We solve with a second-order accurate extension to the ghost fluid/level set method that we developed in Macklin and Lowengrub (2005). Please see Appendix A for new enhancements we have made to the method to satisfy $[\alpha \nabla u \cdot \mathbf{n}] = 0$ on the boundary Σ.

The pressure boundary condition requires an accurate curvature discretization. In Macklin (2003) and Macklin and Lowengrub (2005), we found that standard curvature discretizations are inaccurate and unstable near singularities that result from morphological change. In all our numerical simulations, we use a second-order accurate curvature discretization (in two dimensions) that we developed in Macklin and Lowengrub (2006) to overcome these problems.

We update the position of the interface Σ by solving the PDE

$$\frac{\partial \varphi}{\partial t} + \widetilde{V} \left| \nabla \varphi \right| = 0, \tag{48}$$

where $\widetilde{V}(\mathbf{x},t)$ is an extension of V off of the tumor boundary Σ such that $\widetilde{V} \equiv V$ on Σ. We construct $\widetilde{V}$ using the bilinear extrapolation we developed in Macklin and Lowengrub (2005). As described in Macklin (2003) and Macklin and Lowengrub (2005), we filter the high-frequency variations from $\widetilde{V}$ to attain second-order accuarcy without a third-order CFL condition.

Lastly, we keep φ as a distance function ($|\nabla \varphi| \sim 1$) by solving the PDE

$$\varphi_\tau - \text{sign}(\varphi^0)\left(1 - |\nabla \varphi|\right) = 0 \tag{49}$$

to steady-state, where τ is pseudo-time and φ^0 is the level set function prior to reinitialization (Osher and Sethian, 1988; Malladi et al., 1995, 1996; Adalsteinsson and Sethian, 1999; Sethian, 1999; Osher and Fedkiw, 2001, 2002; Sethian and Smereka, 2003). We solve the PDE's in (48) and (49) with the third-order total variation-diminishing Runge-Kutta method (Gottlieb and Shu, 1997; Gottlieb et al., 2001) and the fifth-order WENO method (Jiang and Shu, 1996; Jiang and Peng, 2000).

3.2 Convergence of the Numerical Method

To evaluate the convergence of our extended numerical method, we simulated two-dimensional tumor growth with $D = 100$, $\mu = 50$, $G = 20$, $G_N = 1$, $N = 0.35$, and $A = 0$, and with a complex initial shape. (See the first frame of Figure A.5.) We simulated up to time $t = 0.15$ at three spatial resolutions: $\Delta x \in \{0.04, 0.08, 0.16\}$.

In Figure A.3 we plot the resulting tumor morphology at low resolution ($\Delta x = 0.16$; upper left plot), medium resolution ($\Delta x = 0.08$; upper right plot), and high resolution ($\Delta x = 0.04$; lower left plot). In all three plots, the dark region denotes the necrotic core Ω_N where $\sigma \leq N$. In the lower right plot of Figure A.3, we compare the position of the tumor boundary for all three resolutions: the dotted curve is for $\Delta x = 0.16$, the dashed curve shows $\Delta x = 0.08$, and the solid curve gives $\Delta x = 0.04$. As we can see, there are considerable differences in the positions of the necrotic core and tumor boundary between the low- and medium-resolution plots, but far fewer differences between the medium- and high-resolution plots; this is indicative of fast convergence. In this and all plots hereafter, white regions correspond to Ω_H, which consists of the ECM, noncancerous cells, and any other material outside of the tumor. Black regions denote the necrotic core Ω_N, and gray regions show the viable portion Ω_V of the tumor.

Defining the order of convergence (of the interface position) similarly to Macklin and Lowengrub (2005) (but measuring error over the entire computational domain, rather than in a band near the tumor boundary), the order of convergence for this example was 2.22, thereby demonstrating that our numerical method is capable of accurately simulating tumor growth, even when faced with complex morphologies.

4 Numerical Results

We now investigate the effects of the tumor microenvironment on the morphology and growth patterns of two-dimensional, avascular tumors growing into piecewise homogeneous tissues. In all simulations, we set the apoptosis parameter $A = 0$ because the tumors are assumed to ignore inhibitory signals for self-destruction (apoptosis). We numerically compute the solutions using a computational mesh with $\Delta x = \Delta y = 0.08$. All tumors are simulated to a scaled nondimensional time of $T = G\,t = \lambda_M t' = 20$, where t' is dimensional time. (The dimensional time is given by $t' = T/\lambda_M$.) Because $\lambda_M^{-1} \sim 1$ day, this nondimensional time allows us to compare tumors of varying simulated genotypes at fixed physical times. (e.g., $T = 20 \approx 20$ days.)

We shall characterize the effects of the modeled tumor microenvironment on growth by presenting a morphology diagram. (Figure A.4.) We simulate growth over a wide range of microenvironmental parameters (D and μ) with $G = 20$, $G_N = 1$, and $N = 0.35$, each with identical initial shape as in the first frame of Figure A.5. Recall that D and μ characterize the relative nutrient diffusivity and biomechanical responsiveness of the exterior tissue, G measures the tumor aggressiveness (proliferation compared to cellular adhesion), G_N characterizes the rate of degradation of the necrotic core, and N is the threshold nutrient level for tumor cell viability.

Later in this paper, we shall consider the effect of G, G_N, and N. We let $D \in \{1, 50, 100, \infty\}$ and $\mu \in \{0.25, 1, 50, \infty\}$. When $D = \infty$, we set $\sigma \equiv 1$ in non-encapsulated regions of Ω_H and only solve the Poisson equation for σ in Ω and the encapsulated portions of Ω_H (with diffusion constant 1). Likewise, when $\mu = \infty$, we set $p \equiv 0$ in non-encapsulated regions of Ω_H and only solve the Poisson equation for p in Ω and the encapsulated portions of Ω_H (with mobility 1). In Figure A.4, we plot the shape of each tumor at time $T = 20.0$. In all figures, the black regions denote Ω_N where the tumor is necrotic, the gray regions show the viable tumor region Ω_V, and the white regions correspond to Ω_H, which consists of the ECM, noncancerous cells, and any other material outside of the tumor.

On the horizontal axis, we vary the nutrient diffusivity of the surrounding tissue; as D increases from left to right, the simulated microenvironment varies from nutrient-poor to nutrient-rich. On the vertical axis, we vary the mobility of the surrounding material; as μ increases from bottom to top, the microenvironment ranges from low-mobility to high-mobility. The greater the mobility μ, the greater the ability of the external, non-cancerous tissue to respond to the pressure generated by the growing tumor, and tumor cells are more able to penetrate the tissue.

We observe three distinct tumor morphologies through this broad range of simulated tissue types. In the nutrient-poor regime on the left side of the diagram, tumors demonstrate *fragmenting growth*, characterized by the repeated breakup of the tumor in response to the low nutrient level. The nutrient-rich, low-mobility regime in the bottom right of the morphology diagram is characterized by *fingering growth*, where buds develop on the tumor boundary that invade the surrounding tissue, forming long, invasive fingers. The nutrient-rich, high-mobility regime in the top right of the diagram demonstrates *compact/hollow growth*, where the tumors tend to grow into spheroids and typically form abscesses filled with noncancerous tissue and fluid, similar to a necrotic core. As we shall discuss further in Section 5, these morphologies are similar to those observed experimentally *in vitro* by Frieboes et al. (2006b). See Figure A.18.

We have found that the tumor morphologies in the morphology diagram in Figure A.4 are qualitatively similar when recomputed with different genetic characteristics (modeled by A, G, G_N, and N), although, as we demonstrate in Section 4.2, large changes in the genetic parameter values can shift the morphology from one type to another. Therefore, a tumor's morphology depends primarily upon the characteristics of the microenvironment. We shall demonstrate this by investigating the three major tumor morphologies in the following sections.

To better characterize the morphological characteristics of a tumor, we define

$$\mathcal{S} = \frac{(\text{Perimeter})^2}{4\pi \text{ Area}} \qquad \text{(shape parameter)} \tag{50}$$

$$\mathcal{LS} = \frac{2 \text{ Area}}{\text{Perimeter}} \qquad \text{(length scale)}. \tag{51}$$

The shape parameter $\mathcal{S}$ is a measure of how noncircular a tumor fragment is. Note that $\mathcal{S} \geq 1$, and $\mathcal{S}$ increases as a tumor fragment is deformed away from a circle. The length scale $\mathcal{LS}$ is a measure of the smallest dimension of a tumor fragment. For example, for a rectangular fragment with width W and length L, $\mathcal{LS} = LW/(L+W)$, and $\mathcal{LS} \sim W$ if $W \ll L$. To describe tumors comprised of multiple fragments, we calculate $\mathcal{S}$ and $\mathcal{LS}$ for each individual fragment and aggregate the results with a fragment volume-weighted average.

4.1 Fragmenting Growth into Nutrient-Poor Microenvironments

In Figure A.5, we show the evolution of a tumor growing into a high-mobility, nutrient-poor tissue, where $D = 1$ and $\mu = \infty$. Here, $G = 20$, $G_N = 1$, $N = 0.35$, and $A = 0$. Due to the low nutrient diffusivity D, the nutrient

level lies below N in much of the tumor microenvironment. Accordingly, a large portion of the tumor becomes necrotic and is broken down by enzymes, leading to early fragmentation. (See $T = 10.0$ in Figure A.5.)

In each tumor fragment, cell proliferation is faster on the outer side (toward the outer boundary of Ω_H) where the nutrient level is highest. (See Figure A.6 to see the nutrient concentration near a typical tumor fragment.) On the opposite side of each fragment, the nutrient level is lowest, leading to slow proliferation and necrosis. The net result is preferential growth of the tumor fragment away from the nutrient-depleted center of the computational domain. In the nutrient-poor microenvironment, it is advantageous for the fragments to elongate, thereby increasing the surface area of the fragments and allowing better access to nutrient. (See $T = 20.0$ and $T = 30.0$ in Figure A.5.) Eventually, when a tumor fragment grows sufficiently long, necrosis causes the fragment to break into multiple satellite fragments which are temporarily stabilized by cellular adhesion, and the process repeats. (See $T = 50.0$, $T = 60.0$, and $T = 70.0$ in Figure A.5.)

We can gain a more detailed understanding of this repeating elongation-fragmentation cycle by examining the evolution of $\mathcal{S}$ and $\mathcal{LS}$ in the top left plot in Figure A.7. Initially, the shape parameter $\mathcal{S}$ (solid line) is large but drops rapidly as cell-cell adhesion pulls cells together and shrinks high-frequency perturbations in the tumor boundary. Thereafter, the shape parameter steadily rises as the tumor fragments elongate and become increasingly noncircular. At the same time, the length scale (dashed line) decreases because the width of the fragments decreases as they elongate. Whenever a fragment becomes sufficiently noncircular, the shape parameter $\mathcal{S}$ peaks, and decay of the necrotic core breaks the fragment into multiple smaller pieces. After the break, the cell-cell adhesion causes the new fragments to coalesce into spheroids, resulting in a rapid drop in $\mathcal{S}$ and an increase in the length scale $\mathcal{LS}$. Consequently, $\mathcal{S}$ reaches a peak when $\mathcal{LS}$ reaches a local minimum, and vice versa. As the trend repeats, $\mathcal{S}$ and $\mathcal{LS}$ trace out a "sawtooth" pattern in Figure A.7 that is characteristic of fragmenting tumor growth. In fact, the formation of smaller fragments at more frequent time intervals can be observed as smaller sawteeth superimposed on the overall pattern.

The repeated elongation-fragmentation cycle is observed in tumor growth into lower-mobility, nutrient-poor regions as well. In Figure A.8, we compare the tumor morphology at $T = 60.0$ and $T = 70.0$ for a high-mobility tissue (left plot: $\mu = \infty$) and a lower-mobility tissue (right plot: $\mu = 1$); repeated fragmentation is observed in both cases. When growing into a lower-mobility region, however, it is more difficult for the tumor to deform into highly-elongated fragments. Instead, the individual fragments grow into larger spheroids before deforming and breaking into new fragments. All these trends can be observed in the evolution of the shape parameter $\mathcal{S}$ (solid curve) and $\mathcal{LS}$ (dashed curve)

on the top right plot of Figure A.7. The characteristic "sawtooth" pattern can still be seen in the shape parameter and length scale. However, the oscillations in the shape parameter are much smaller, which reflects the difficulty in forming large deformations when growing into low-mobility tissue. The lack of smaller, superimposed sawteeth indicates fewer topology changes and more localized growth, which is seen in the smaller number of tumor fragments in Figure A.8. Because the tumor fragments grow to form larger spheroids before deforming and fragmenting, the length scale also tends toward higher values in the low-mobility tissue case.

When examining the internal structure of tumors growing in nutrient-poor ($D = 1$) tissues, we find that the high-mobility ($\mu = \infty$; lower left plot in Figure A.7) and low-mobility ($\mu = 1$; lower right plot in Figure A.7) tissue cases are quite similar. The viable and necrotic volume fractions rapidly approach limiting values that are nearly identical for both tumors, at approximately 70% viable area and 30% necrotic area. The similarity of the limiting values is consistent with our analysis in Section 2.6, where we found that the necrotic volume fraction does not depend upon the tissue cellular mobility μ for steady-state tumor spheroids. Unlike the case of circular growth where the volume fractions only stabilize once a (global) steady-state has been achieved, the necrotic volume fraction here stabilizes even during growth because the tumor features apparently reach local equilibrium between cell proliferation and necrosis. Interestingly, the necrotic volume fraction is quite similar to that predicted for spheroids with $D = 1$ (see Section 2.6), albeit somewhat lower, which indicates that the deformation of the larger tumor fragments marginally increases access to nutrient.

Tumors growing into nutrient-poor microenvironments demonstrate repeated fragmentation through a wide range of mitosis rates (governed by the parameter G) and necrotic tissue degradation rates (G_N). In Figure A.9, we show the tumor morphology at time $T = 20.0$ for a variety of values of G and G_N and $\mu = D = 1$. Tumor fragmentation is observed in almost all cases, particularly for fast-proliferating, aggressive tumors with higher values of G. An increased aggressiveness (G) increases the rate of tumor fragmentation. Similarly, increasing the rate of necrotic tissue degradation (G_N) tends to destabilize the tumor, also leading to an increased rate of fragmentation. However, this effect is highly nonlinear: if G_N is large relative to G, then proliferation, necrosis, and cellular adhesion can balance to maintain spheroids and prevent further tumor fragmentation. This can be seen in the $G = 1$, $G_N = 10$ case in Figure A.9: the tumor splits into two spheroids that reach a steady size while preferentially growing outward toward higher nutrient levels. We note that for sufficiently low levels of tumor aggressiveness (e.g., $G = 0.10$), tumor instability decreases until the steady-state configuration is tumor spheroids, as predicted in Cristini et al. (2003) for non-necrotic tumors. (Results not shown.)

As was predicted in Section 2.6 in the case of tumor spheroids, we found that the volume fractions of viable and necrotic tissue were largely independent of the tumor aggressiveness parameter G and the microenvironmental characteristics (D and μ) and were primarily functions of N and G_N. For $N = 0.35$ and $G_N = 0.10$, necrotic tumor cells were degraded very slowly; consequently, the majority of the tumor (approximately 80%) was composed of necrotic tissue and 20% by viable cells. Fixing $N = 0.35$ and increasing G_N, the volume fraction occupied by necrotic tumor tissue steadily decreased, at approximately 30% for $G_N = 1$ and 5% for $G_N = 10$.

In the cases where the tumors have not fragmented by $T = 20.0$, moderate-to-significant deformation still occurs, and fragmentation is likely at a later time. The occurrence of repeated tumor fragmentation over a broad range of G and G_N demonstrates that in the nutrient-poor regime, tumor morphology is largely determined by the characteristics of the surrounding microenvironment, while the genetic characteristics of the tumor (G, G_N, A, and N) determine the size and rate of evolution of the tumor. In addition, increasing the apoptosis rate A to positive values results in similar morphological behavior, only with more rapid tumor fragmentation and a greater number of fragments. (Results not shown.)

We examined the impact of N on the morphology of tumor growth in the nutrient-poor regime, and the results for $N \in \{0.175, 0.350, 0.700\}$ are given in Figure A.10, where $D = \mu = G_N = 1$ and $G = 20$. For all three values of N, the tumor demonstrated repeated fragmentation (top row of Figure A.10), and therefore all demonstrated the characteristic sawtooth pattern in $\mathcal{S}$ and $\mathcal{LS}$. (Bottom row of Figure A.10.) As N increases, the volume fraction of the tumor undergoing necrosis increases from approximately 20% ($N = 0.175$) to roughly 30% ($N = 0.350$) to nearly 40% ($N = 0.700$), leading to a decrease in the overall size and spread of the tumor fragments (top row of Figure A.10).

The finding that tumor morphology in the nutrient-poor regime depends primarily upon the tumor microenvironment (μ and D) and not the tumor's genetic characteristics (N, G_N, and G) has important implications for cancer treatment. In anti-angiogenic therapy, drugs (e.g., Avastin) are supplied to prevent the neovascularization of the growing tumor and the surrounding tissue. As we have seen, the resulting nutrient-poor microenvironment may cause the tumors to fragment and invade nearby tissues, particularly for growth in higher-mobility tissues. This can negate the positive effects of antiangiogenic therapy and may lead to recurrence and metastasis. This result is consistent with the findings of Cristini et al. (2005), who suggested that combining antiangiogenic therapy with adhesion therapy may counteract the negative problems associated with tumor fragmentation in the nutrient-poor regime.

4.2 Invasive, Fingering Growth

In Figure A.11, we show the evolution of a tumor growing into a low-mobility, nutrient-rich tissue, where $D = 50$ and $\mu = 1$. As in the previous section, $G = 20$ $G_N = 1$, and $N = 0.35$. Because nutrient readily diffuses through the surrounding tissue Ω_H, the tumor is initially non-necrotic, allowing for unchecked growth and the development of buds on the tumor periphery that protrude into the surrounding tissue. (See time $T = 10$ in Figure A.11.) Due to the cell-cell adhesion (modeled by the pressure jump in (18)), the proliferation-induced mechanical pressure is greatest surrounding any protusions of the tumor into the healthy tissue and approximately zero near flatter regions of the tumor boundary. Because the cellular motility μ is low in the noncancerous tissue, the individual cells and the extracellular matrix cannot move to equilibrate the pressure. As a result, the cellular velocity field is mostly parallel to the buds, in spite of adequate nutrient levels between the growing buds. (See the left plot of Figure A.12 for the nutrient concentration between two growing buds, and the right plot for the corresponding pressure field.) This makes it difficult for buds to merge, leading to the formation of long, invasive fingers. (See $T = 30.0$ to $T = 50.0$ in Figure A.11.) The net effect is highly-invasive growth into the surrounding tissue. (See $T = 50.0$ in Figure A.11.)

Within the nutrient-rich, low-mobility tissue regime, we examined two levels of tissue mobility ($\mu \in \{0.25, 1\}$) and three nutrient diffusivities ($D \in \{50, 100, \infty\}$), for a total of six combination of mobility and nutrient diffusivity. In the top left plot in Figure A.13, we show the evolution of the shape parameter $\mathcal{S}$ for these six simulations. We found that the shape parameter depended primarily upon the tissue mobility: the three lower-mobility tissue examples ($\mu = 0.25$, thin dotted, dashed, and solid curves) had an overall higher shape parameter than the higher-mobility tissue ($\mu = 1$, thick dotted, dashed, and solid curves), which reflects a higher degree of deformation. This trend is indeed observed in the morphologies along the $\mu = 0.25$ row of Figure A.4. This is because the lower the tissue mobility, the more difficult it is for cells in the healthy tissue to overcome the cell-cell and cell-ECM adhesion and move to equilibrate pressure variations, and the more difficult it is for the ECM to deform in response to the pressure, allowing for the formation of sharper corners and greater shape instabilities.

This trend is also reflected in the tumor perimeters in the lower left plot of Figure A.13: overall, the larger deformation in the lower-mobility tissue simulations leads to overall larger perimeters in the low-mobility tissue cases (thin curves) than in the higher-mobility tissue cases (thicker curves). As a result of the increased surface area, the low-mobility tissue tumors had greater access to nutrient. This leads to a surprising result: the increased morphological instability from growing into lower-mobility tissues improves

access to nutrient and leads to larger tumors, as can be seen in the lower right plot in Figure A.13; for each fixed nutrient diffusivity, the volume of the viable area of each tumor was larger for the lower-mobility tissue simulation ($\mu = 0.25$) than for the corresponding higher-mobility tissue example ($\mu = 1$). For all examples, the shape parameter steadily rose as a function of time, which reflects the increasing shape instability as the tumors invade the surrounding tissue; this is characteristic of invasive, fingering growth. This has implications for therapies that target cell-cell and cell-ECM adhesiveness: if the therapy decreases the mobility in the surrounding microenvironment (by increasing the cell-cell or cell-ECM adhesiveness or rendering the ECM more rigid), then invasive, fingering growth into the surrounding tissue is likely. Likewise, any treatment that decreases the permeability of the host tissue to tumor cells may lead to an increase in tumor invasiveness.

In the upper right plot of Figure A.13, we see that the length scale $\mathcal{LS}$ is most strongly dependent upon the nutrient diffusivity D, and largely independent of the tissue mobility μ. As the nutrient diffusivity increases, nutrient is better able to diffuse between the growing fingers, allowing the nutrient to penetrate farther into the fingers. This allows the tumor to support thicker fingers, which can be seen in the increased length scale parameter $\mathcal{LS}$ for higher values of D. In all cases, the length scale tended toward a roughly fixed value, which demonstrates that each tissue can support a specific finger thickness.

As was predicted in Section 2.6 for tumor spheroids and observed in the fragmenting growth regime, the volume ratios of the tumor were nearly independent of the tumor microenvironment. We examined the viable and necrotic volume fractions for growing tumors with $\mu \in \{0.25, 1\}$ and $D \in \{50, 100, \infty\}$. In all cases, the volume fractions quickly stabilized, with the viable rim comprising approximately 65% of the tumors and the remaining 35% being made up of necrotic cells. This necrotic volume fraction is slightly less than that predicted for tumor spheroids with $D = 50$ (approximately 37% for spheroids), which again reflects the fact that the tumor's morphological response to the microenvironment increases its access to nutrient.

In Figure A.14, we examine the effect of the tumor aggressiveness parameter G and the necrotic degradation parameter G_N on the invasive, fingering morphology. We fix $D = 50$, $\mu = 1$, $N = 0.35$, and take $0.1 \leq G_N \leq 10.0$ and $1 \leq G \leq 100$. For lower tumor aggressiveness values ($G = 1$) and $G_N \geq 1$, the fingering effect was significantly reduced, resulting in more stable, tubular-shaped tumors, an effect that has been observed in experiments (Frieboes et al., 2006b). These structures form because tumor cell proliferation (the numerator of G) and cell-cell adhesion (the denominator of G) are roughly in balance when $G = 1$. The competition between proliferation and adhesion smooths but does not completely prevent shape instabilities, which may continue to grow. For sufficiently large values of G, the invasive fingering mor-

phology was observed in all simulated tumors. For lower values of G_N (left column in Figure A.14), the low rate of degradation of the necrotic tumor tissue leads to the formation of very wide fingers; this morphology may be better described as a collection of spheroids. As G_N is increased, the necrotic core is degraded more quickly, leading to a decreased finger thickness, less stable morphology, and more aggressive tissue invasion. As G_N is increased toward $G_N = 10$ (right column in Figure A.14), the finger thickness is decreased to the point where the tumor periodically breaks into fragments and then reconnects, leading to the encapsulation of noncancerous tissue (white enclosed regions). This morphology, which we refer to as compact/hollow, is characterized by the presence of a large abscess containing a mixture of necrotic cells, fluid, noncancerous ECM, and cellular debris, much like a necrotic core. A long-time simulation of a tumor with the compact/hollow morphology can be seen in Figure A.15 with a different value of μ; this morphology will be examined in greater detail in the following section. The effect of G_N on growth is seen to be non-monotonic: increasing G_N at first limits the size of the tumor by decreasing the thickness of the invasive fingers and limiting the overall spread of the tumor, but after a certain point, instability breaks the tumor and allows greater spread through the surrounding noncancerous tissue. For example, for $G = 10$, the total viable area at time $T = 20$ drops from 103.3404 when $G_N = 0.10$ to 93.3156 for $G_N = 1.0$, then increases to 133.7360 for $G_N = 10$.

Lastly, we studied the effect of N on the invasive fingering growth regime by simulating with $N \in \{0.175, 0.350, 0.700\}$, $G = 20$, $G_N = 1$, $D = 1$, and $\mu = 1$. As in the fragmenting case, we found that varying N changes the tumor evolution quantitatively but not qualitatively. As N increases, the thickness of the viable rim and the overall spread of the tumor decrease, and the necrotic volume fraction increases ($N = 0.175$: approximately 25%; $N = 0.35$: nearly 35%; $N = 0.70$: over 40%.).

4.3 Compact, Hollow Growth

In Figure A.15, we show the evolution of a tumor growing into a high-mobility ($\mu = 50$), nutrient-rich ($D = 100$) tissue, where $G = 20$, $N = 0.35$, and $G_N = 1$. In the beginning ($T = 0.0$ to $T = 5.0$ in Figure A.15), growth is very similar to the invasive, fingering case. Because the noncancerous tissue is nutrient-rich, the tumor only develops a necrotic core after an initial period of growth, after which shape instabilities (buds) appear. However, because the noncancerous tissue has a greater mobility μ, the cells and extracellular matrix in the surrounding noncancerous tissue are more free to move and relieve the pressure caused by the growing tumor. Consequently, the buds on the outer edge of the tumor do not invade the surrounding tissue, but instead flatten and periodically merge, encapsulating healthy tissue in the process ($T = 10.0$

to $T = 20.0$ in Figure A.15), a process that has been previously observed in boundary integral simulations of tumor growth (Cristini et al., 2003). In the meantime, necrotic tissue on the inside boundary of the tumor continues to degrade, leading to the formation of a large abscess in the tumor core filled with a mixture of noncancerous tissue and cellular debris ($T = 15.0$ and $T = 20.0$ in Figure A.15). We expect that in reality, any noncancerous cells contained in the abscess may also undergo necrosis, and due to the presence of matrix degrading enzymes in the tumor, encapsulated ECM should be degraded. This suggests an evolution similar to those seen for smaller values of G. We shall further investigate these effects in a future work.

Within the nutrient-rich, high-mobility regime, we examined two levels of mobility ($\mu \in \{50, \infty\}$) and three nutrient diffusivities ($D \in \{50, 100, \infty\}$). In all plots, $G = 20$, $G_N = 1$, $N = 0.35$, and $A = 0$, thin curves denote lower-mobility ($\mu = 50$) simulations, and thick curves give higher-mobility ($\mu = \infty$) simulations. In all plots, the dotted lines are for $D = 50$, the dashed lines are $D = 100$, and the solid lines correspond to $D = \infty$.

In the top left plot of Figure A.16, we plot the evolution of the shape parameter $\mathcal{S}$ for all these simulations. In all cases, the shape parameter increased in an eratic manner, which is indicative of frequent increases in morphological complexity. This is a reflection of the frequent formation and merger of buds, and of the encapsulation of noncancerous tissue by the growing tumor seen in Figure A.15, and the behavior is similar for all simulations except for the $D = 50$, $\mu = \infty$ case. In that case, the encapsulation of tissue is much less frequent, and the behavior is similar to fragmenting growth: the tumor breaks into two halves, each of which resembles the elongated fragments observed in fragmenting growth. (See the uppermost tumor in Figure A.17 for a closer view of this morphology.) For all six simulations, the values of $\mathcal{S}$ are generally higher than for the other growth regimes. This is because the tumor consists of two concentric boundaries like a ring: a complex, outer boundary with many shape instabilities, and a necrotic inner boundary. Accordingly, the compact/hollow tumors have a much greater ratio of perimeter to area. The length scale $\mathcal{LS}$, shown in the top-right plot of Figure A.16, generally decreases for all simulations, with signs of tending toward a limiting value. This is because as the tumors grow, a characteristic rim thickness emerges, but the frequent encapsulation of noncancerous tissue causes the length scale to fluctuate in time.

We examined the viable and necrotic volume fractions for each of these simulations. As was the case with fragmenting and fingering growth, the percentages were nearly identical (approximately $65\% - 75\%$ viable and $30\% - 35\%$ necrotic) for all cases throughout most of the simulation time. The necrotic volume fraction was substantially less than the approximate 37% predicted for tumor spheroids with $D \geq 10$, and also generally less than that observed

for invasive, fingering tumors with equal values of D. This is because the buds on the tumor periphery increase access to nutrient, are small enough to have very little necrotic tissue, and thereby reduce the necrotic volume fraction.

In Figure A.17, we examine the effect of the tumor aggressiveness G and the necrotic degradation rate G_N on the compact tumor morphology. In all these simulations, we fix $D = 50$, $\mu = \infty$, and $N = 0.35$. For lower values of G (bottom of the plot), the tumors remain in compact morphologies that fail to encapsulate noncancerous tissue, although shape instabilities may occur at long times. When $G = 1$, cell proliferation (numerator of G) and adhesion (denominator of G) are roughly in balance, which shrinks but does not completely prevent shape instabilities. For larger values of G (upper portion of the plot), the cell proliferation rate outstrips cell-cell adhesion, resulting in folds in the outer tumor surface that encapsulate noncancerous tissue. For fixed values of G, we see that increasing the necrotic tissue degradation rate parameter G_N shrinks the necrotic volume fraction of the tumors. In the cases where noncancerous tissue has been encapsulated ($G > 1$), increasing G_N increases the size of the central tumor abscess.

Lastly, as in the fragmenting and fingering cases, we found that varying N changes the tumor evolution quantitatively but not qualitatively. As N increases, the thickness of the viable rim decreases, the necrotic volume fraction increases, and morphological instability also increases.

5 Discussion and Future Work

In this work, we have extended previous models of tumor growth and developed a framework to investigate the interaction between avascular solid tumors and their microenvironments during growth. In particular, we model the perfusion of nutrient through the tumor and the surounding microenvironment, the build-up of pressure in the tissue from the proliferation of cancerous cells, cell-cell and cell-ECM adhesion, and the loss of tumor volume due to necrosis.

Following previous models of solid tumor growth (Greenspan, 1976; McElwain and Morris, 1978; Adam, 1996; Byrne and Chaplain, 1996a,b; Chaplain, 2000), the genetic characteristics of the tumors are modeled by a small number of nondimensional parameters. One parameter, G, measures the tumor aggressiveness. A second parameter A measures the susceptibility of tumor cells to apoptosis, a third parameter N gives the critical nutrient level for tumor cell necrosis, and a fourth parameter G_N measures the enzymatic breakdown of necrotic tumor cells.

The biophysical characteristics of the microenvironment are modeled by a pa-

rameter D that measures the nutrient diffusivity of the host tissue relative to the diffusivity in the tumor, and a mobility parameter μ. The parameter D can be used to model normoxia (high D) or hypoxia (low D) in the microenvironment. The parameter μ models the combined effects of adhesion (both cell-cell and cell-ECM) and the capacity of the ECM to deform in response to pressure induced by tumor cell proliferation. The proliferative (oncotic) pressure serves as a simple model of tissue stress.

Using this framework, we investigated the effect of the microenvironment on tumor growth with a variety of genetic parameter combinations. In almost all cases, we found that the qualitative features of tumor morphologies are primarily determined by the microenvironmental parameters (D and μ). The parameters that characterize the tumor genetics (G, G_N, N, and A) generally affect quantitative aspects of the tumor progression, such as the size, the amount of invasion into the host tissue, the rate of growth, and the degree of morphological instability.

We found that the internal structure of the tumors (i.e., the necrotic and viable volume fractions of the tumors) depends primarily upon D, G_N, and N, and very little upon μ and G. Furthermore, we found that these volume fractions tend toward constant values even during growth, which indicates the emergence of characteristic feature sizes within the growing tumors and suggests a local equilibrium is attained. This is in contrast to the case of tumor spheroids, whose volume fractions only stabilize once a global steady state is established.

We observed three distinct morphologies: fragmenting, invasive/fingering, and compact/hollow growth. If the microenvironment is nutrient-poor (low D), tumors tend to break into small fragments and spread throughout the microenvironment, regardless of the cellular mobility μ. Within this nutrient-poor growth regime, decreasing the microenvironmental mobility μ (by increasing the noncancerous cell-cell and cell-ECM adhesion or increasing the rigidity of the ECM) decreases the extent of the fragmentation and slows invasion into the surrounding tissue, but does not completely prevent the hypoxia-induced morphological instability. We note that unstable tumor morphologies in the nutrient-poor regime have also been observed by Anderson (2005) and Cristini et al. (2005).

The invasive, fingering morphology was found in cases of growth into nutrient-rich, low-mobility microenvironments. We found that increasing nutrient perfusion does not prevent this invasive morphology, and the lower the microenvironmental mobility μ, the greater the degree of morphological instability and invasiveness. Tumors growing into nutrient-rich, high-mobility tissues develop compact/hollow morphologies. A hallmark of this growth regime is the formation and merger of buds on the tumor periphery, which leads to the en-

capsulation of noncancerous regions Ω_H and the formation of a large abscess (a mixture of noncancerous cells, ECM, fluid, and cellular debris) in the tumor interior. Qualitatively, the interior abscess is similar to a necrotic core.

Within each of these three growth regimes, we investigated the effects of the genetic parameters G, G_N, and N. We found that lowering G, which corresponds to decreasing the tumor proliferation rate and/or increasing the tumor cell-cell adhesiveness, can stabilize growth, an effect that is already known. On the other hand, increasing G_N, which corresponds to an increased rate of degradation of the necrotic regions, tends to destabilize growth. Increasing N leads to smaller tumors.

Our results have important implications for therapy. Since decreasing the nutrient levels in the microenvironment tends to increase tumor fragmentation and invasion into the surrounding tissue, caution must be exercised when considering anti-angiogenic therapies. If this therapy is aimed at destroying the neovasculature as much as possible, this could lead to the adverse effect of inducing morphological instability that may lead to additional tumor fragmentation and invasion. Indeed, a number of experimental studies have now shown that anti-angiogenic therapies may increase the tendency of tumors to fragment and invade surrounding host tissue. (e.g., Sakamoto (1987), Rubinstein et al. (2000), DeJaeger et al. (2001), E. Rofstad and Halso (2002), Seftor et al. (2002), Lamszus et al. (2003), and Bello et al. (2004).) Conversely, we found that increasing the nutrient levels in the microenvironment leads to greater morphological stability and increased compactness of the tumor, thereby rendering the tumors more resectable. Consequently, our results support the contention of Cristini et al. (2005) that treatments that seek to normalize the tumor vasculature (by selectively "pruning" weak blood vessels with targeted anti-angiogenic therapy) may stabilize the tumor morphology by providing the tumor with increased access to nutrient. Since such treatments may also increase the accessibility of the tumors to chemotherapeutic agents (Jain, 2001; Sinek et al., 2004), our results provide additional support for the use of targeted anti-angiogenic therapy as an adjuvant therapy to chemotherapy and resection. This is currently under investigation.

Our findings may have particular significance for breast cancer treatment when considered alongside other known effects of hypoxia. In our simulations, hypoxia, such as that caused by anti-angiogenic therapy, increases tumor morphological instability and invasiveness. In recent findings by Erler et al. (2006), it was shown that hypoxia upregulates lysl oxidase (LOX), which, in turn, is associated with estrogen receptor (ER)-negative breast cancer cells. This is of clinical importance, because ER-negative breast cancers are unsuited to hormone-based therapies and generally have worse prognosis (Chi et al., 2006). Therefore, when indiscriminant anti-angiogenic therapy is applied to breast cancer, it may lead to the fragmentation of the tumor into smaller,

more invasive tumors which are resistant to further treatment.

As was pointed out by Cristini et al. (2005), another approach to therapy is to use anti-invasive drugs such as Met inhibitors (Boccaccio et al., 1998; Bardelli et al., 1999; Morotti et al., 2002) or hepatocyte growth factor antagonists (Date et al., 1998; Michieli et al., 1999) in addition to anti-angiogenic therapies. Such therapies affect the cell-cell and cell-ECM adhesive properties of the tumor. A recent experimental study on mouse models of malignant glioma shows that fragmentation can be prevented, and the elimination of tumor satellites may be achieved by a combined anti-angiogenic and anti-invasive therapy (Bello et al., 2004). In the nutrient-poor growth regime, increasing the cell-cell and cell-ECM adhesion of the microenvironment (i.e., reducing μ) can help to limit the rate of tumor fragmentation and the extent of tissue invasion. Decreasing the permeability of the microenvironmental ECM to tumor cells by other means such as making the extra-tumor ECM more dense, stiffer, and less able to support tumor cell movement could also attain this effect.

Interestingly, the *opposite* approach is warranted in the nutrient-rich growth regime. In this regime, increasing μ in the extra-tumor ECM decreases the extent of invasive fingering. Thus, in a nutrient-rich tissue, an approach to therapy is to increase the permeability of the microenvironment Ω_H to tumor cells. This can be accomplished by decreasing the cell-cell and cell-ECM adhesion in the microenvironment Ω_H (while leaving tumor cells unaffected), or equivalently, by increasing the tumor cell-cell and cell-ECM adhesion. We note that this effect may also be attained by decreasing the stiffness or density of the surrounding ECM. Such subtleties highlight the importance of considering tumor-microenvironment interactions when planning therapies that affect the adhesive and mechanical properties of the tumor, the surrounding tissue, or both.

It is important to ask whether the morphologies predicted here in our study occur during real tumor growth. In fact, by characterizing the range of behavior in the tumor growth model and comparing to experiments, we may predict physically relevant parameter ranges. For example, in our studies, we have taken the aggressiveness parameter $G \geq 1$. In simulations not presented, we have found that taking $G < 1.0$ with apoptosis $A = 0.0$ may result in stable, circular tumor morphologies during avascular growth. We note that in recent work, Frieboes et al. (2006b) predicted a lower value of G for morphologic instability ($0.6 \leq G \leq 0.9$ for marginal stability, and $G > 0.9$ for very unstable behavior) based upon an approximation of a similar theoretical model of spheroid growth that accounted only for apoptosis and not necrosis. This analysis overpredicts instability.

Interestingly, all of the morphologies found in this work have been seen in an *in vitro* tumor growth study performed as part of a joint experimen-

tal/computational investigation of tumor growth by Frieboes et al. (2006b). In that study, tumor spheroids were placed in a solution containing various levels of glucose and fetal bovine serum (FBS). The levels of glucose and FBS were both found to affect the tumor progression and morphology. When the glucose level was low, the *in vitro* tumors shed cells and fragmented. The degree to which this occurred depended upon the level of FBS. When the FBS level was low, growth was slow and a limited amount of tumor fragmentation was observed. See the lower left plot of Figure A.18 for a characteristic image. When the level of FBS was high, the growth was faster, the tumors developed bulbous protrusions, and many fragments were formed. See the upper left plot of Figure A.18. When the glucose level was high and the FBS level was low, invasive fingers developed, and fragmentation was limited. See the lower right plot of Figure A.18. When the levels of glucose and FBS were both high, the tumors had roughly spherical shapes with bulbous protrusions on the surface. The tumors shed cells that strongly connected with each other, creating networks. See the upper right plot in Figure A.18. Very interestingly, if FBS can be correlated with the permeability of the ECM to tumor cells (in this case, the ECM is created by the tumor cells themselves), then this behavior correlates very well with our predictions using the parameters D and μ (high glucose and FBS levels correspond to large D and μ, respectively). This will be a subject of future study.

Now that the general capabilities of the basic model have been demonstrated, we are working to extend the realism of our simulator by modeling additional biophysical effects, including more detailed modeling of the internal structure of the tumors and the surrounding tissue. In collaboration with A.R.A. Anderson, M.A.J. Chaplain, V. Cristini, and S.R. McDougall, we are fully coupling our tumor growth model with the DATIA (dynamic adaptive tumour-induced angiogenesis) model of McDougall et al. (2006). With our improved models, we plan to further investigate the dynamics of tumor growth, the complex interplay between the microenvironment and the tumor, and possibilties for improved therapies. With an improved model in hand, we hope to calibrate it to specific cancers, allowing for specific predictions that can be verified in a laboratory setting. Our ultimate goal is the development of efficient, effective, and eventually individualized treatment regimens.

6 Acknowledgements

We thank the National Science Foundation Division of Mathematical Sciences and the UCI Department of Mathematics for their financial support. We thank Vittorio Cristini and Hermann Frieboes at the UCI Department of Biomedical Engineering for valuable discussions and for their generosity in providing unpublished experimental data from their 2006 study in Frieboes et al. (2006b).

We thank Alexander "Sandy" Anderson and Mark Chaplain at the University of Dundee and Steven McDougall at Heriot Watt University for valuable discussions. We thank the reviewers for their comments, which helped improve the presentation of this paper.

A Improvements to the Ghost Fluid Method

We now describe a second-order accurate extension of the ghost fluid method (Fedkiw et al., 1999; Liu et al., 2000; Gibou et al., 2002, 2003; Gibou and Fedkiw, 2005) to solve the Poisson-like system

$$\begin{aligned} \alpha\nabla^2 u = f_1(\mathbf{x},t) + f_2(\mathbf{x},t)u \quad & \text{in} \quad \Omega \text{ and } \Omega_H & \text{(A.1)} \\ [u] = g(\mathbf{x},t) \quad & \text{on} \quad \Sigma & \text{(A.2)} \\ [\alpha\nabla u\cdot\mathbf{n}] = 0 \quad & \text{on} \quad \Sigma & \text{(A.3)} \\ u \equiv u_O \quad & \text{on} \quad \partial(\Omega\cup\Omega_H) & \text{(A.4)} \end{aligned}$$

on arbitrary domains embedded in a rectangular domain Ω_{comp}, where

$$\alpha = \begin{cases} \alpha_T \text{ in } \Omega \\ \alpha_H \text{ in } \Omega_H, \end{cases} \tag{A.5}$$

and α_T and α_H are positive constants.

In Macklin and Lowengrub (2005), we developed a second-order accurate extension of the ghost fluid method to solve this system in the case where $\Omega_H = \emptyset$ and $[\alpha\nabla u\cdot\mathbf{n}]$ is not specified on the boundary Σ. We now extend the method to solve the present system.

We discretize each partial derivative of $\alpha\nabla^2 u$ separately, and so we can focus our attention on the discretization of αu_{xx} at a node point $x_i \in \Omega$. If $x_{i-1} = x_i - \Delta x$ and $x_{i+1} = x_i + \Delta x$ are both contained in Ω, then we discretize $\alpha_T u_{xx}$ with the standard second-order stencil:

$$\alpha_T u_{xx} = \alpha_T \frac{u(x_{i-1}) - 2u(x_i) + u(x_{i+1})}{\Delta x^2} + \mathcal{O}(\Delta x^2). \tag{A.6}$$

However, if $x_{i+1} \in \Omega_H$, then the boundary must separate x_i and x_{i+1} at some point $x_\Sigma = x_i + \theta\Delta x$, where $0 < \theta < 1$. In this scenario, we must modify our stencil by first extending the solution in Ω to a "ghost fluid point" $\widehat{u}(x_{i+1})$ in Ω_H; we replace $u(x_{i+1})$ by $\widehat{u}(x_{i+1})$ in the discretization of $\alpha_T u_{xx}$ in (A.6).

See Figure A.19. We proceed by a quadratic extrapolation of u from $u(x_{i-2})$, $u(x_{i-1})$, and $u(x_\Sigma)\big|_\Omega = \lim_{x \uparrow x_\Sigma} u(x)$ to $\widehat{u}(x_{i+1})$.

We discretize (A.2) by

$$u(x_\Sigma)\big|_\Omega = u(x_\Sigma)\big|_{\Omega_H} + g(x_\Sigma, t), \tag{A.7}$$

where the jump notation is as defined in (9). If g is a function that is only defined at mesh points, then we evaluate $g(x_\Sigma, t)$ by cubic interpolation of $g(x_{i-1}, t)$, $g(x_i, t)$, $g(x_{i+1}, t)$, and $g(x_{i+2}, t)$.

We discretize (A.3) by

$$\alpha_T \frac{u(x_\Sigma)\big|_\Omega - u(x_{i-1})}{(1+\theta)\Delta x} = \alpha_H \frac{u(x_{i+2}) - u(x_\Sigma)\big|_{\Omega_H}}{(2-\theta)\Delta x}. \tag{A.8}$$

This discretization is similar to the discretization of Liu et al. (2000), although we use different points in the discretization for improved numerical stability. We note that this discretization approximates the jump condition $[\alpha \nabla u \cdot \mathbf{n}]$ as $[\alpha u_x] = 0$ and $[\alpha u_y] = 0$ when discretizing the x- and y-derivatives. (In three dimensions, $[\alpha u_z] = 0$ as well.) This is equivalent to assuming that the interface cuts the stencil at a right angle. Wherever this assumption is inaccurate, any tangential jump in $\alpha \nabla u$ is partially smeared out numerically. This limitation is characteristic of all current ghost fluid methods and is a trade-off for the dimension-by-dimension simplicity of the discretization. We are currently investigating solutions to this problem.

By combining (A.7) and (A.8), we can completely eliminate $u(x_\Sigma)\big|_\Omega$ and $u(x_\Sigma)\big|_{\Omega_H}$ from the discretization of $\alpha_T u_{xx}$. This allows the discretization of the entire Poisson system to be written in the form of a linear system $L\mathbf{u} = \mathbf{b}$, which can be solved by standard linear solvers. In our work, we used the stabilized biconjugate gradient method BiCG-Stab(2). (van der Vorst, 1992; Sleijpen et al., 1994; Duff et al., 1998) The case where $x_{i-1} \notin \Omega$ is handled analogously, and the discretization of $\alpha_H u_{xx}$ is similar. We discretize the far-field boundary condition (A.4) as in Macklin and Lowengrub (2005), where we define $\Omega_O = \Omega_{\text{comp}} \backslash \overline{(\Omega \cup \Omega_H)}$ to be the far field tissue and set

$$\frac{1}{\Delta x^2} u(x_i) = \frac{1}{\Delta x^2} u_O, \qquad \mathbf{x} \in \Omega_O. \tag{A.9}$$

This dimension-by-dimension discretization allows the use of the same method in both 2D and 3D problems, transforms the difficult problem of solving a

diffusional problem on an arbitrary domain to the simpler problem of diffusion on a rectangle, and is easy to extend to greater accuracy.

In our testing, we found this method to be second-order accurate. (See Section 3.2 for convergence testing results.) We are investigating the numerical smearing of tangential jumps in $\alpha \nabla u$, but our technique is currently the state-of-the art in solving Poisson-like systems on arbitrary evolving domains when using the ghost fluid approach. An alternative approach for overcoming the tangential smearing problem is the immersed interface method, which requires the use of local coordinates (based on the normal and tangential directions of the interface) to modify the discretization (Leveque and Li, 1994).

References

Abbott, R. G., Forrest, S., Pienta, K. J., 2006. Simulating the Hallmarks of Cancer. Artif. Life 12 (4), 617–34.

Adalsteinsson, D., Sethian, J., 1999. The Fast Construction of Extension Velocities in Level Set Methods. J. Comput. Phys. 148 (1), 2–22.

Adam, J., 1996. General aspects of modeling tumor growth and the immune response. In: Adam, J., Bellomo, N. (Eds.), A survey of models on tumor immune systems dynamics. Birkhauser, Boston, MA, pp. 15–87.

Alarcón, T., Byrne, H. M., Maini, P. K., 2003. A cellular automaton model for tumour growth in inhomogeneous environment. J. Theor. Biol. 225 (2), 257–274.

Ambrosi, D., Guana, F., 2006. Stress-modulated growth. Math. Mech. Solids(in press).

Ambrosi, D., Mollica, F., 2002. On the mechanics of a growing tumor. Int. J. Eng. Sci. 40, 1297–1316.

Ambrosi, D., Mollica, F., 2004. The role of stress in the growth of a multicell spheroid. J. Math. Biol. 48, 477–499.

Ambrosi, D., Preziosi, L., 2002. On the closure of mass balance models for tumor growth. Math. Mod. Meth. Appl. Sci. 12 (5), 737–754.

Anderson, A. R. A., 2005. A Hybrid Mathematical Model of Solid Tumour Invasion: The Importance of Cell Adhesion. IMA Math. App. Med. Biol. 22, 163–186.

Anderson, A. R. A., Chaplain, M. A. J., 1998. Continuous and discrete mathematical models of tumor-induced angiogenesis. Bull. Math. Biol. 60, 857–900.

Anderson, A. R. A., Chaplain, M. A. J., Lowengrub, J. S., Macklin, P., McDougall, S., 2006. Nonlinear Simulation of Tumour Invasion and Angiogenesis. Bull. Math. Biol.(in preparation).

Araujo, R. P., McElwain, D. L. S., 2004a. A history of the study of solid tumor

growth: The contribution of mathematical modeling. Bull. Math. Biol. 66, 1039–1091.

Araujo, R. P., McElwain, D. L. S., 2004b. A linear-elastic model of anisotropic tumor growth. Euro. J. Appl. Math. 15, 365–384.

Araujo, R. P., McElwain, D. L. S., 2005. A mixture theory for the genesis of residual stresses in growing tissues II: Solutions to the biphasic equations for a multicell spheroid. SIAM J. Appl. Math. 66, 447–467.

Bardelli, A., Basile, M. L., Audero, E., et al., 1999. Concomitant activation of pathways downstream of Grb2 and PI 3-kinase is required for MET-mediated metastasis. Oncogene 18, 1139–46.

Bello, L., Lucini, V., Costa, F., et al., 2004. Combinatorial administration of molecules that simultaneously inhibit angiogenesis and invasion leads to increased therapeutic efficacy in mouse models of malignant glioma. Clin. Cancer Res. 10, 4527–37.

Bellomo, N., de Angelis, E., Preziosi, L., 2003. Multiscale modelling and mathematical problems related to tumor evolution and medical therapy. J. Theor. Medicine 5 (2), 111–136.

Boccaccio, C., Ando, M., Tamagnone, L., et al., 1998. Induction of epithelial tubules by growth factor HGF depends on the STAT pathway. Nature 391, 285–8.

Bredel-Geissler, A., Karbach, U., Walenta, S., Vollrath, L., Mueller-Kleiser, W., 1992. Proliferation associated oxygen consumption and morphology of tumor cells in monolayer and spheroid culture. J. Cell. Phys. 153, 44–52.

Brizel, D. M., Scully, S. P., Harrelson, J. M., et al., 1996. Tumor oxygenation predicts for the likelihood of distant metastases in human soft tissue sarcoma. Cancer Res. 56, 941–3.

Byrne, H., Preziosi, L., 2003. Modelling solid tumour growth using the theory of mixtures. Math. Med. Biol. 20, 341–366.

Byrne, H. M., Alarcón, T., Owen, M. R., Webb, S. D., Maini, P. K., 2006. Modeling aspects of cancer dynamics: A review. Phil. Trans. R. Soc. A 364, 1563–1578.

Byrne, H. M., Chaplain, M. A. J., 1996a. Growth of necrotic tumors in the presence and absence of inhibitors. Math. Biosci. 135, 187–216.

Byrne, H. M., Chaplain, M. A. J., 1996b. Modelling the role of cell-cell adhesion in the growth and development of carcinomas. Math. Comput. Model. 24, 1–17.

Byrne, H. M., Matthews, P., 2002. Asymmetric growth of models of avascular solid tumors: exploiting symmetries. IMA J. Math. Appl. Med. Biol. 19 (1), 1–29.

Cairns, R. A., Kalliomaki, T., Hill, R. P., 2001. Acute (cyclic) hypoxia enhances spontaneous metastasis of KHT murine tumors:. Cancer Res. 61, 8903–8.

Carmellet, P., Jain, R. K., 2000. Angiogenesis in cancer and other diseases. Nature 407, 249–257.

Chaplain, M. A. J., 2000. Pattern Formation in Cancer. In: Chaplain, M.

A. J., Singh, G. D., MacLachlan, J. C. (Eds.), On growth and Form: Spatio-temporal pattern formation in Biology. Wiley Series in Mathematical and Computational Biology, New York, NY, pp. 47–70.

Chaplain, M. A. J., Ganesh, M., Graham, I. G., 2001. Spatio-temporal pattern formation on spherical surfaces: numerical simulation and application to solid tumour growth. J. Math. Biol. 42 (5), 387–423.

Chaplain, M. A. J., Graziano, L., Preziosi, L., 2006. Mathematical modelling of the loss of tissue compression responsiveness and its role in solid tumour development. Math. Med. Biol. 23, 192–229.

Chi, J. T., et al., 2006. Gene expression programs in response to hypoxia: Cell type specificity and prognostic significance in human cancers. PLoS Med. 3 (e47).

Cristini, V., Frieboes, H. B., Gatenby, R., Caserta, S., Ferrari, M., Sinek, J., 2005. Morphological instability and cancer invasion. Clin. Cancer Res. 11 (19), 6772–6779.

Cristini, V., Lowengrub, J. S., Nie, Q., 2003. Nonlinear simulation of tumor growth. J. Math. Biol. 46, 191–224.

Date, K., Matsumoto, K., Kuba, K., Shimura, H., Tanaka, M., Nakamura, T., 1998. Inhibition of tumor growth and invasion by a four-kringle antagonist (HGF/NK4) for hepatocyte growth factor. Oncogene 17, 3045–54.

DeJaeger, K., Kavanagh, M. C., Hill, R., 2001. Relationship of hypoxia to metastatic ability in rodent tumors. Br. J. Cancer 84, 1280–1285.

Duff, L. S., Sorensen, D. C., van der Vorst, H. A., Dongarra, J. J., 1998. Numerical Linear Algebra for High-Performance Computers. Society for Industrial and Applied Math, Philadelphia, PA.

E. Rofstad, E., Halso, E., 2002. Hypoxia-associated spontaneous pulmonary metastasis in human melanoma xenographs: involvement of microvascular hotspots induced in hypoxic foci by interleukin. Br. J. Cancer 86 (8), 301–308.

Enam, S. A., Rosenblum, M. L., Edvardsen, K., 1998. Role of extracellular matrix in tumor invasion: migration of glioma cells along fibronectin-positive mesenchymal cell processes. Neurosurgery 42 (3), 599–608.

Enmon Jr., R. M., O'Connor, K. C., Lacks, D. J., Schwartz, D. K., Dotson, R. S., 2001. Dynamics of spheroid self-assembly in liquid overlay culture of DU 145 human prostate cancer cells. Biotech. Bioeng. 72 (6), 579–591.

Erler, J. T., Bennewith, K. L., Nicolau, M., Dornhoefer, N., Kong, C., L, Q.-T., Chi, J.-T. A., Jeffrey, S. S., Siaccia, A. J., 2006. Lysyl oxidase is essential for hypoxia-induced metastasis. Nature 440 (27), 1222–1226.

Esteban, M. A., Maxwell, P. H., 2005. HIF, a missing link between metabolism and cancer. Nature Med. 11, 1047–8.

Fedkiw, R. P., Aslam, T., Merriman, B., Osher, S., 1999. A Non-Oscillatory Eulerian Approach to Interfaces in Multimaterial Flows (the Ghost Fluid Method). J. Comput. Phys. 152 (2), 457–492.

Festjens, N., Vanden Berghe, T., Vandenabeele, P., 2006. Necrosis, a well-orchestrated form of cell demise: Signalling cascades, important mediators

and concomitant immune response. Biochim. Biophys. Acta 1757 (9-10), 1371–1387.

Freyer, J. P., 1988. Role of necrosis in regulating the growth saturation of multicellular spheroids. Cancer Res. 48 (9), 2432–9.

Frieboes, H. B., Wise, S. M., Lowengrub, J. S., Cristini, V., 2006a. Three-dimensional Diffuse-Interface Simulation of Multispecies Tumor Growth-II: Investigation of Tumor Invasion. Bull. Math. Biol.(in review).

Frieboes, H. B., Zheng, X., Sun, C.-H., Tromberg, B., Gatenby, R., Cristini, V., 2006b. An integrated computational/experimental model of tumor invasion. Canc. Res. 66 (3), 1597–1604.

Friedl, P., Wolf, K., 2003. Tumour-Cell Invasion and Migration: Diversity and Escape Mechanisms. Nat. Rev. Cancer 3, 362–374.

Galaris, D., Barbouti, A., Korantzopoulos, P., 2006. Oxidative Stress in Hepatic Ischemia-Reperfusion Injury: The Role of Antioxidants and Iron Chelating Compounds. Current Pharma. Design 12, 2875–2890.

Garber, K., 2004. Energy Boost: The Warburg effect returns in a new theory of cancer. JNCI 96, 1805–6.

Gatenby, R. A., Gawlinski, E. T., 1996. A reaction-diffusion model of cancer invasion. Cancer Res. 56 (24), 5745–5753.

Gatenby, R. A., Gawlinski, E. T., 2003. The Glycolytic Phenotype in Carcinogenesis and Tumor Invasion: Insights through Mathematical Models. Cancer Res. 63, 3847–3854.

Gibou, F., Fedkiw, R., 2005. A Fourth Order Accurate Discretization for the Laplace and Heat Equations on Arbitrary Domains, with Applications to the Stefan Problem. J. Comput. Phys. 202 (2), 577–601.

Gibou, F., Fedkiw, R., Caflisch, R., Osher, S., 2003. A level set approach for the numerical simulation of dendritic growth. J. Comput. Phys. 19, 183–199.

Gibou, F., Fedkiw, R., Cheng, L. T., Kang, M., 2002. A Second Order Accurate Symmetric Discretization of the Poisson Equation on Irregular Domains. J. Comput. Phys. 176 (1), 205–227.

Gottlieb, S., Shu, C. W., 1997. Total Variation Diminishing Runge-Kutta Schemes. Math. Comp. 67 (221), 73–85.

Gottlieb, S., Shu, C. W., Tadmor, E., 2001. Strong Stability-Preserving High-Order Time Discretization Methods. SIAM Review 43 (1), 89–112.

Greenspan, H. P., 1976. On the Growth and Stability of Cell Cultures and Solid Tumors. J. Theor. Biol. 56, 229–242.

Hanahan, D., Weinberg, R. A., 2000. The hallmarks of cancer. Cell 100 (1), 57–70.

Haroon, Z., Peters, K. G., Greenberg, C. S., Dewhirst, M. W., 1999. Angiogenesis and Blood Flow in Solid Tumors. In: Teicher, B. (Ed.), Antiangiogenic Agents in Cancer Therapy. Humana Press, Totowa, NJ, Ch. 1, pp. 3–21.

Hashizume, H., Baluk, P., Morikawa, S., et al., 2000. Openings between defective endothelial cells explain tumor vessel leakiness. Am. J. Pathol. 156, 1363–80.

Hedlund, T. E., Duke, R. C., Miller, G. J., 1999. Three dimensional spheroid

cultures of human prostate cancer cell lines. Prostate 41 (3), 154–165.
Hockel, M., Schlenger, K., Aral, B., Mitze, M., Schaffer, U., Vaupel, P., 1996. Association between tumor hypoxia and malignant progression in advanced cancer of the uterine cervix. Canc. Res. 56 (19), 4509–4515.
Hoeckel, M., Vaupel, P., 2001. Tumor hypoxia: definitions and current clinical, biologic, and molecular aspects. J. Natl. Cancer Inst. 93, 266–276.
Hogea, C. S., Murray, B. T., Sethian, J. A., 2006. Simulating complex tumor dynamics from avascular to vascular growth using a general level-set method. J. Math. Biol. 53 (1), 86–134.
Hotary, K., Allen, E. D., Brooks, P. C., Datta, N. S., Long, M. W., Weiss, S. J., 2003. Membrane type 1 matrix metalloproteinase usurps tumour growth control imposed by the three-dimensional extracellular matrix. Cell 114, 33–45.
Jain, R. K., 1990. Physiological Barriers to Delivery of Monoclonal Antibodies and Other Macromolecules in Tumors. Cancer Research (Suppl.) 50, 814s–819s.
Jain, R. K., 2001. Normalizing tumor vasculature with anti-angiogenic therapy: A new paradigm for combination therapy. Nature Medicine 7 (9), 987989.
Jiang, G. S., Peng, D., 2000. Weighted ENO Schemes for Multi-Dimensional Hamilton-Jacobi Equations. SIAM J. Sci. Comput. 21 (6), 2126–2143.
Jiang, G. S., Shu, C. W., 1996. Efficient Implementation of Weighted ENO Schemes. J. Comput. Phys. 126 (2), 202–228.
Jones, A. F., Byrne, H. M., Gibson, J. S., Dold, J. W., 2000. A mathematical model of the stress induced during avascular tumor growth. J. Math. Biol. 40, 473–499.
Kaur, B., Khwaja, F. W., Severson, E. A., Matheny, S. L., Brat, D. J., Van Meir, E. G., 2005. Hypoxia and the hypoxia-inducible-factor pathway in glioma growth and angiogenesis. Neuro-oncol. 7 (2), 134–153.
Kloner, R. A., Jennings, R. B., 2001. Consequences of brief ischemia: stunning, preconditioning, and their clinical implications: part 1. Circulation 104 (24), 2981–2989.
Konopleva, M., Zhao, S. R., Hu, W., Jiang, S. W., Snell, V., Weidner, D., Jackson, C. E., Zhang, X., Champlin, R., Estey, E., Reed, J. C., Andreeff, M., 2002. The anti-apoptotic genes Bcl-X-L and Bcl-2 are over- expressed and contribute to chemoresistance of non- proliferating leukaemic CD34(+) cells. Brit. J. Haematology 118 (2), 521–534.
Lamszus, K., Kunkel, P., Westphal, M., 2003. Invasion as limitation to anti-angiogeneic glioma therapy. Acta Neurochir Suppl 88, 169–177.
Lehmann, A. R., 2001. The xeroderma pigmentosum group D (XPD) gene: one gene, two functions, three diseases. Genes Dev. 15 (1), 15–23.
Lester, R. D., Jo, M., Campana, W. M., Gonias, S. L., 2005. Erythropoietin promotes MCF-7 breast cancer cell migration by an ERK/mitogen-activated protein kinase-dependent pathway and is primarily responsible for the increase in migration observed in hypoxia. J. Biol. Chem. 280 (47),

39273–39277.

Leveque, R., Li, Z., 1994. The Immersed Method for Elliptic Equations with Discontinuous Coefficients and Singular Sources. SIAM J. Numer. Anal. 31 (4), 1019–1044.

Li, X., Cristini, V., Nie, Q., Lowengrub, J. S., 2006. Nonlinear three-dimensional simulation of solid tumor growth. Dis. Cont. Dyn. Sys. B(in review).

Liu, X. D., Fedkiw, R., Kang, M., 2000. A Boundary Condition Capturing Method for Poisson's Equation on Irregular Domains. J. Comput. Phys. 160 (1), 151–178.

Macklin, P., September 2003. Numerical Simulation of Tumor Growth and Chemotherapy. M.S. thesis, University of Minnesota School of Mathematics.

Macklin, P., Lowengrub, J. S., 2005. Evolving interfaces via gradients of geometry-dependent interior Poisson problems: application to tumor growth. J. Comput. Phys. 203 (1), 191–220.

Macklin, P., Lowengrub, J. S., 2006. An improved geometry-aware curvature discretization for level set methods: application to tumor growth. J. Comput. Phys. 215 (2), 392–401.

Malladi, R., Sethian, J. A., Vemuri, B. C., 1995. Shape Modeling with Front Propagation: A Level Set Approach. IEEE Trans. Pattern Anal. Mach. Intell. 17 (2).

Malladi, R., Sethian, J. A., Vemuri, B. C., 1996. A fast level set based algorithm for topology-independent shape modeling. J. Math. Imaging Vision 6, 269–289.

Mallett, D. G., de Pillis, L. G., 2006. A Cellular Automata Model of Tumor-immune System Interactions. J. Theor. Biol. 239 (3), 334–350.

Mansury, Y., Kimura, M., Lobo, J., Deisboeck, T. S., 2002. Emerging Patterns in Tumor Systems: Simulating the Dynamics of Multicellular Clusters with an Agent-based Spatial Agglomeration Model. J. Theor. Biol. 219 (3), 343–370.

McDougall, S. R., Anderson, A. R. A., Chaplain, M. A. J., 2006. Mathematical modelling of dynamic adaptive tumour-induced angiogenesis: Clinical implications and therapeutic targeting strategies. J. Theor. Biol.(in press).

McElwain, D. L. S., Morris, L. E., 1978. Apoptosis as a Volume Loss Mechanism in Mathematical Models of Solid Tumor Growth. Mathematical Biosciences 39, 147–157.

Michieli, P., Basilico, C., Pennacchietti, S., et al., 1999. Mutant Met-mediated transformation is ligand-dependent and can be inhibited by HGF antagonists. Oncogene 18, 5221–31.

Morotti, A., Mila, S., Accornero, P., Tagliabue, E., Ponzetto, C., 2002. K252a inhibits the oncogenic properties of Met, the HGF receptor. Oncogene 21, 4885–93.

Mueller-Kleiser, W., 1997. Three dimensional cell cultures: from molecular mechanisms to clinical applications. Am. J. Physiol. 273, C1109–C1123.

Osher, S., Fedkiw, R., 2001. Level Set Methods: An Overview and Some Recent

Results. J. Comput. Phys. 169 (2), 463–502.
Osher, S., Fedkiw, R., 2002. Level Set Methods and Dynamic Implicit Surfaces. Springer, New York, NY.
Osher, S., Sethian, J. A., 1988. Fronts propagating with curvature-dependent speed: algorithms based on Hamilton-Jacobi formulations. J. Comput. Phys. 79, 12–49.
Pennacchietti, S., Michieli, P., Galluzzo, M., Giordano, S., Comoglio, P., 2003. Hypoxia promotes invasive growth by transcriptional activation of the *met* protooncogene. Cancer Cell 3, 347–361.
Postovit, L. M., Adams, M. A., Lash, G. E., Heaton, J. P., Graham, C. H., 2002. Oxygen-mediated regulation of tumor cell invasiveness. Involvement of a nitric oxide signaling pathway. J. Biol. Chem. 277, 35730–7.
Pouysségur, J., Dayan, F., Mazure, N. M., 2006. Hypoxia signalling in cancer and approaches to enforce tumour regression. Nature 441 (25), 437–443.
Quaranta, V., Weaver, A. M., Cummings, P. T., Anderson, A. R. A., 2005. Mathematical Modeling of Cancer: The future of prognosis and treatment. Clinica Chimica Acta 357 (2), 173–9.
Ramanathan, et al., 2005. Perturbational profiling of a cell-line model of tumorigenesis by using metabolic measurements. PNAS 102, 5992–7.
Ravandi, F., Estrov, Z., 2006. Eradication of leukemia stem cells as a new goal of therapy in leukemia. Clin. Cancer Res. 12 (2), 340–344.
Rofstad, E., Rasmussen, H., Galappathi, K., Mathiesen, B., Nilsen, K., Graff, B. A., 2002. Hypoxia promotes lymph node metastasis in human melanoma xenografts by up-regulating the urokinase-type plasminogen activator receptor. Cancer Res. 62, 1847–53.
Roose, T., Netti, P. A., Munn, L. L., Boucher, Y., Jain, R., 2003. Solid stress generated by spheroid growth estimated using a linear poroelastic model. Microvascular Res. 66, 204–212.
Rubinstein, J. L., Kim, J., T, O., et al., 2000. Anti-VEGF antibody treatment of glioblastoma prolongs survival but results in increased vascular cooption. Neoplasia 2, 306–314.
Sakamoto, G., 1987. Infiltrating carcinoma: major histological types. In: Page, D. L., Anderson, T. J. (Eds.), Diagnostic Histopathology of the Breast. Churchill-Livingstone, London, United Kingdom, pp. 219–222.
Sanga, S., Sinek, J. P., Frieboes, H. B., Fruehauf, J. P., Cristini, V., 2006. Mathematical modeling of cancer progression and response to chemotherapy. Expert. Rev. Anticancer Ther. 6 (10), 1361–76.
Sanson, B. C., Delsanto, P. P., Magnano, M., Scalerandi, M., 2002. Effects of anatomical constraints on tumor growth. Phys. Rev. E 64 (2), 21903ff.
Schmeichel, K. L., Weaver, V. M., Bissel, M. J., 1998. Structural cues from the tissue microenvironment are essential determinants of the human mammary epithelial cell phenotype. J. Mammary Gland Biol. and Neoplasia 3 (2), 201–213.
Seftor, E. A., Meltzer, P. S., Kirshmann, D. A., et al., 2002. Molecular determinants of human uveal melanoma invasion and metastasis. Clin. Exp.

Metastasis 19, 233–246.
Sethian, J. A., 1999. Level Set Methods and Fast Marching Methods. Cambridge University Press, New York, NY.
Sethian, J. A., Smereka, P., 2003. Level set methods for fluid interfaces. Ann. Rev. of Fluid Mech. 35, 341–372.
Sinek, J., Frieboes, H., Zheng, X., Cristini, V., 2004. Two-dimensional Chemotherapy Simulations Demonstrate Fundamental Transport and Tumor Response Limitations Involving Nanoparticles. Biomed. Microdev. 6 (4), 197–309.
Sleijpen, G. L. G., van der Vorst, H. A., Fokkema, D. R., 1994. bicgstab(ℓ) and other hybrid Bi-CG methods. Numer. Algorithms 1 (7), 75109.
Sussman, M., Smereka, P., Osher, S., 1994. A level set approach for computing solutions to incompressible two-phase flow. J. Comput. Phys. 114, 146ff.
van der Vorst, H. A., 1992. BI-CGSTAB: A fast and smoothly converging variant of BI-CG for the solution of nonsymmetric linear systems. SIAM J. Sci. Stat. Comput. 13 (2), 631–644.
Vaupel, P., Kallinowski, F., Okunieff, P., 1989. Blood flow, oxygen and nutrient supply, and metabolic microenvironment of human tumours: a review. Cancer Res. 49, 6449–6465.
Wise, S., Frieboes, H., Cristini, V., 2006a. Three-dimensional simulation of the growth of a multispecies tumor via a diffuse interface approach. Bull. Math. Biol.(in review).
Wise, S. M., Lowengrub, J. S., Frieboes, H. B., Cristini, V., 2006b. Three-dimensional Diffuse-Interface Simulation of Multispecies Tumor Growth-I: Numerical Method. Bull. Math. Biol.(in review).
Zheng, X., Wise, S. M., Cristini, V., 2005. Nonlinear simulation of tumor necrosis, neo-vascularization and tissue invasion via an adaptive finite-element/level set method. Bull. Math. Biol. 67, 211–259.

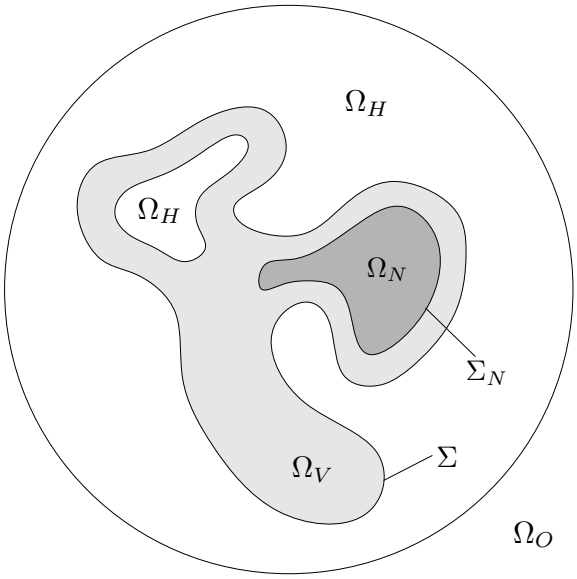

Fig. A.1. Diagram of the regions in and near a growing tumor: the tumor Ω is comprised of viable (proliferating and quiescent) cells in Ω_V and necrotic cells in Ω_N. The noncancerous tissue surrounding tissue surrounding the tumor, denoted by Ω_H, is affected by the growing tumor, and portions of Ω_H may be encapsulated by the growing tumor. Lastly, the noncancerous tissue Ω_O is not affected by the growing tumor.

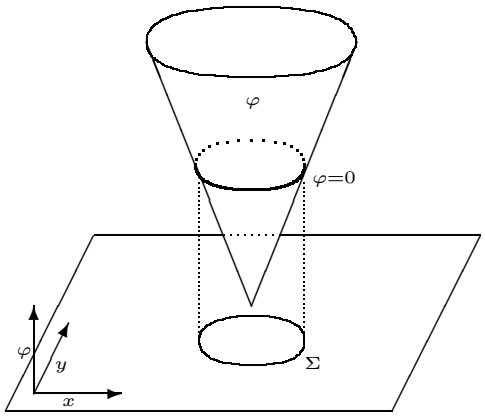

Fig. A.2. Representing an ellipse Σ as the zero contour of a level set function φ.

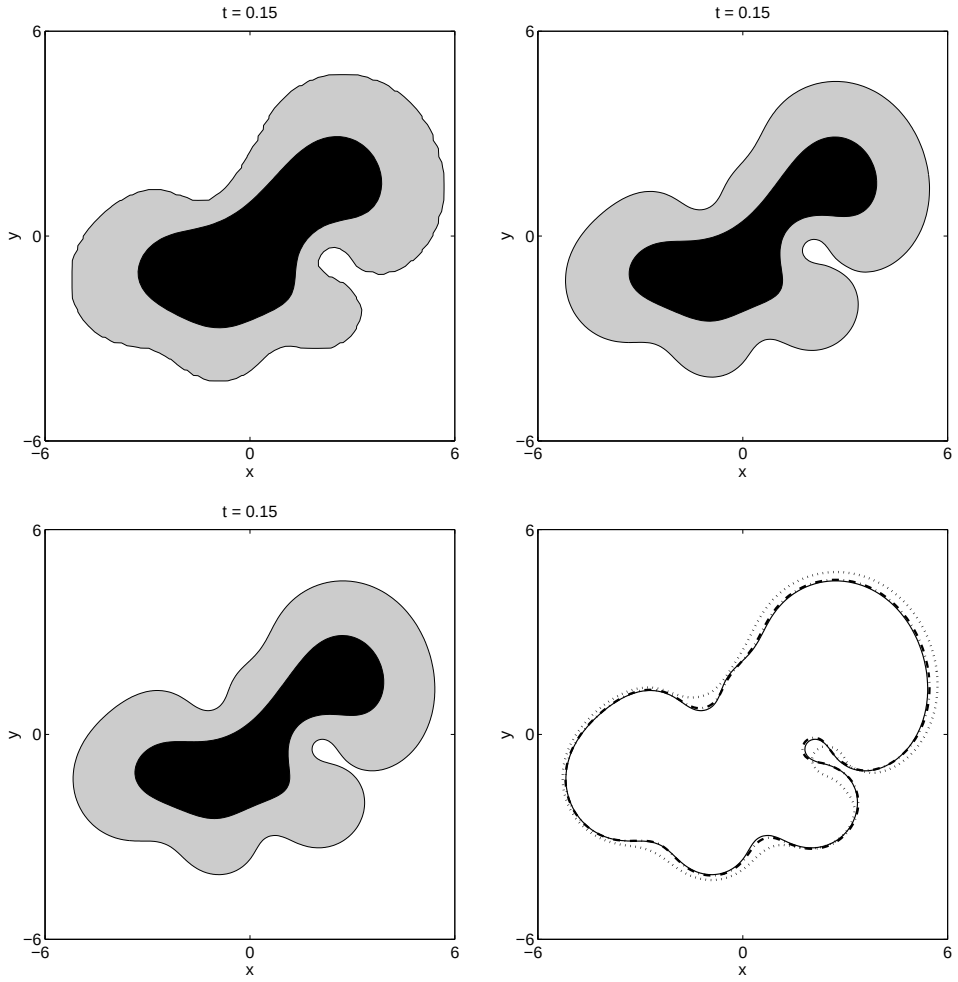

Fig. A.3. Numerical Convergence: Tumor morphology at $t = 0.15$ at low resolution (upper left), medium resolution (upper right), and high resolution (lower left). The dark region denotes the necrotic core Ω_N where $\sigma \leq N = 0.35$, and the gray regions show the viable region Ω_V. In the lower right plot, we compare the position of the tumor boundary at low resolution (dotted curve), medium resolution (dashed curve), and high resolution (solid curve).

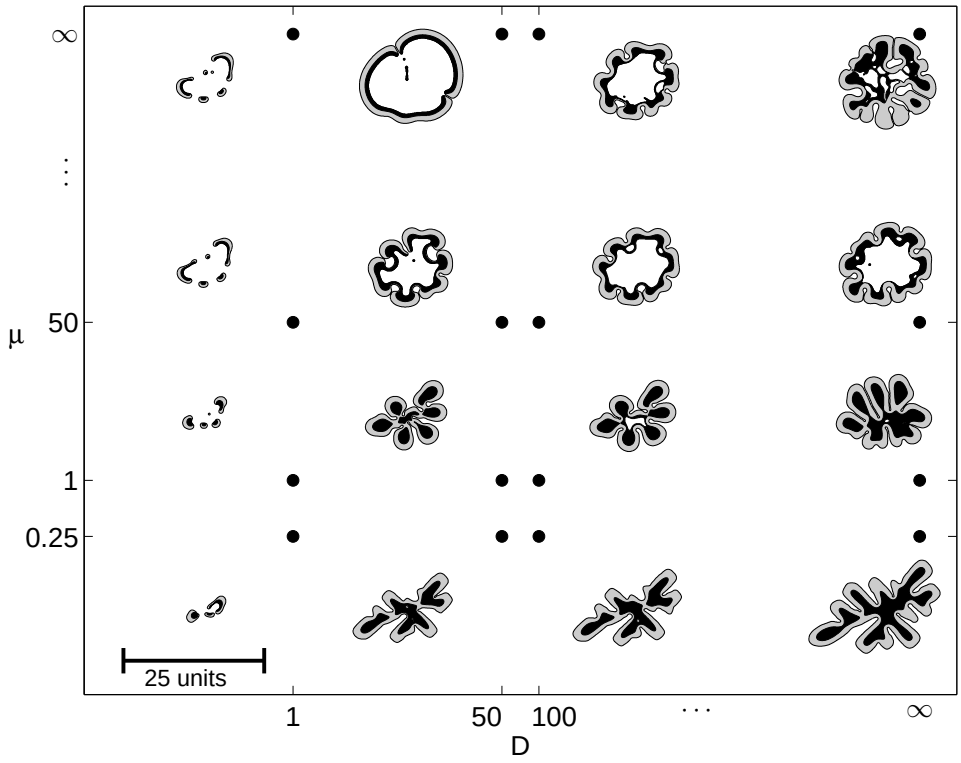

Fig. A.4. Tumor morphological response to the microenvironment. The external tissue nutrient diffusivity D increases from left to right, and the external tissue mobility μ increases from bottom to top. Three major morphologies are observed: fragmenting growth (left), invasive fingering (lower right), and compact/hollow (upper right). All tumors are plotted to the same scale, where the indicated length is $25L \approx 0.5$ cm.

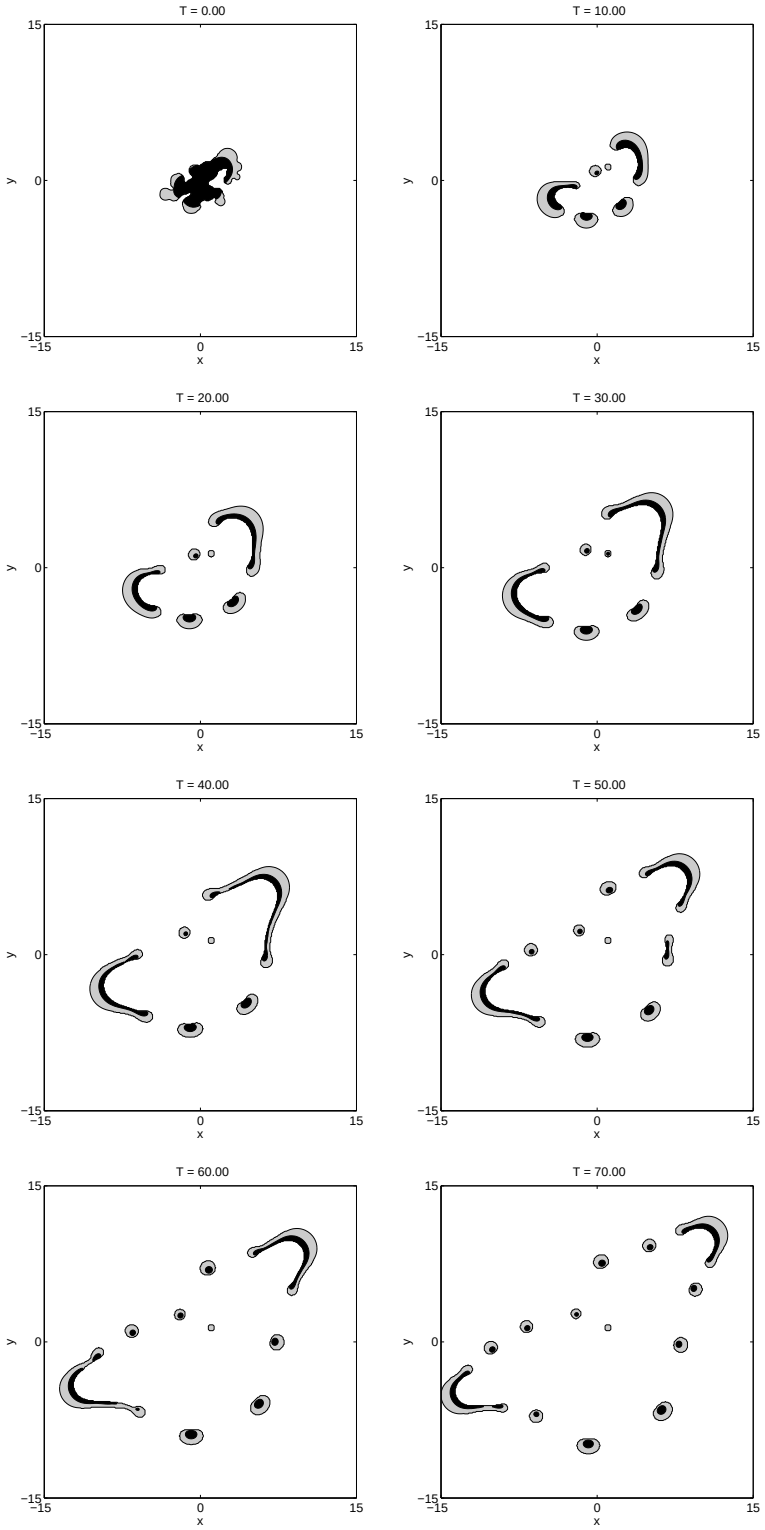

Fig. A.5. Long time simulation of fragmenting growth into nutrient-poor ($D = 1$), high-mobility ($\mu = \infty$) tissue. Plots are in $T = 10.0$ increments, $G = 20$, $G_N = 1$, $N = 0.35$, and $A = 0$.

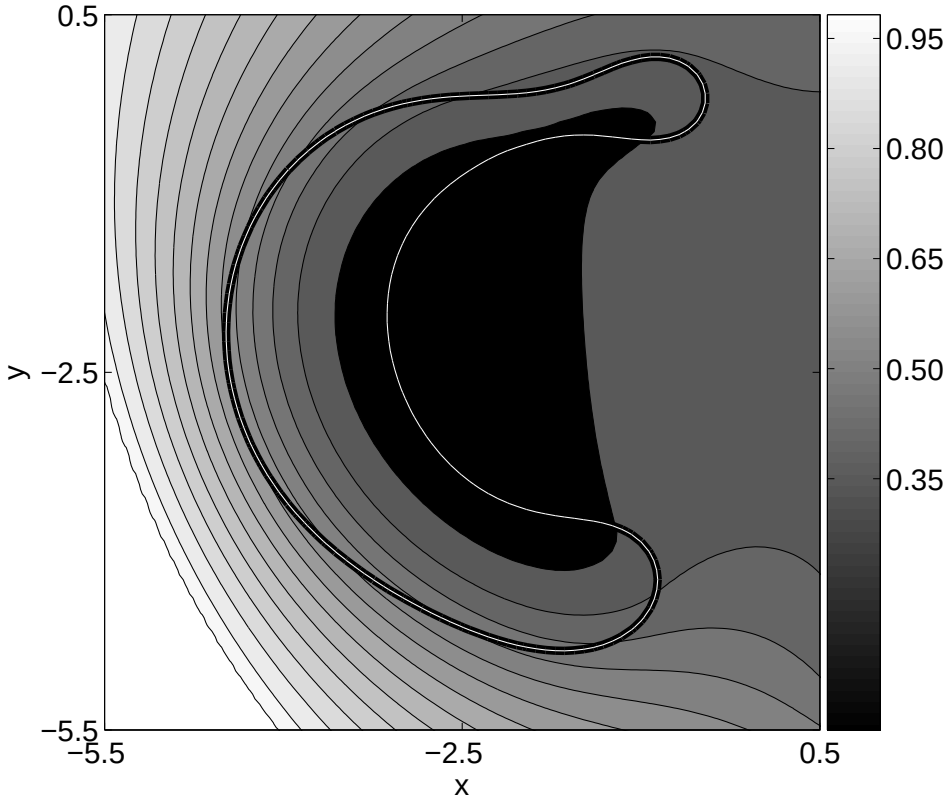

Fig. A.6. Contours of the nutrient concentration near a tumor fragment from the previous figure at $T = 20.0$. The black regions denote nutrient-starved regions where $\sigma < N$. Notice the large variation in nutrient level from the left side of the fragment to the right.

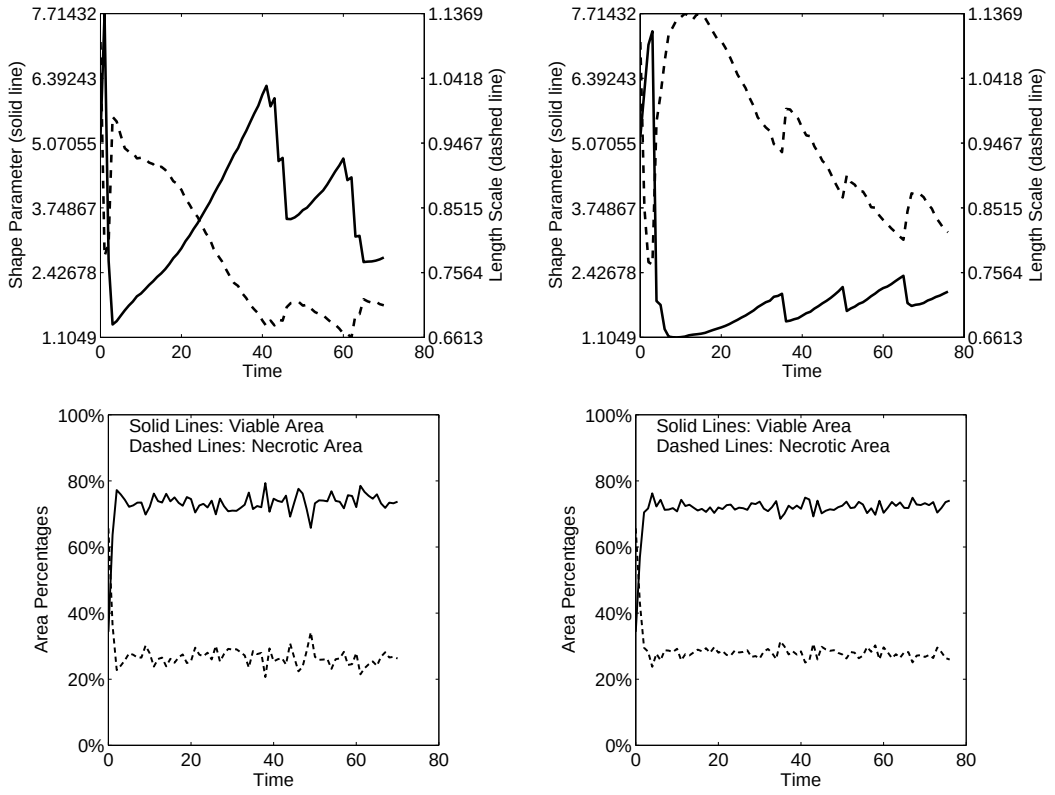

Fig. A.7. **Top Row:** Evolution of the shape parameter $\mathcal{S}$ (solid curves) and length scale $\mathcal{LS}$ (dashed curves) for fragmenting tumor growth into nutrient-poor tissue. The left plot is for growth into high-mobility tissue ($D = 1$, $\mu = \infty$), and the right plot is for growth into low-mobility tissue ($D = 1$, $\mu = 1$). **Bottom Row:** Evolution of the viable and necrotic volume fractions for the high-mobility case ($\mu = \infty$; left plot) and low-mobility case ($\mu = 1$; right plot).

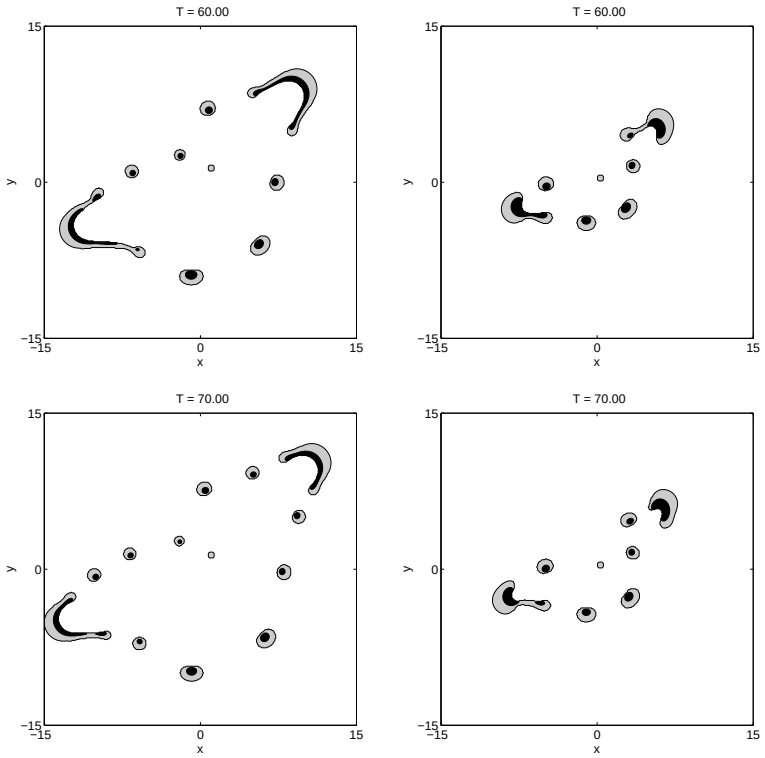

Fig. A.8. Comparison of fragmenting tumor growth into high-mobility tissue ($\mu = \infty$, left plots) and low-mobility tissue ($\mu = 1$, right plots) at $T = 60.0$ and $T = 70.0$.

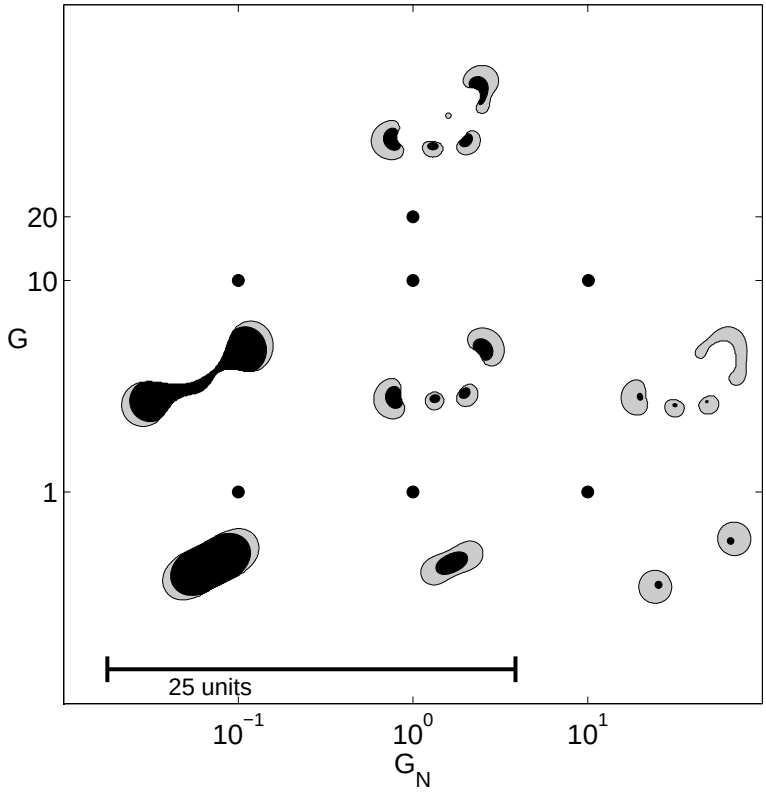

Fig. A.9. Parameter study in G and G_N for fragmenting tumor growth into nutrient-poor, low-mobility tissue ($D = 1$, $\mu = 1$). The tumor aggressiveness parameter G increases from bottom to top, and the necrotic degradation parameter G_N increases from left to right.

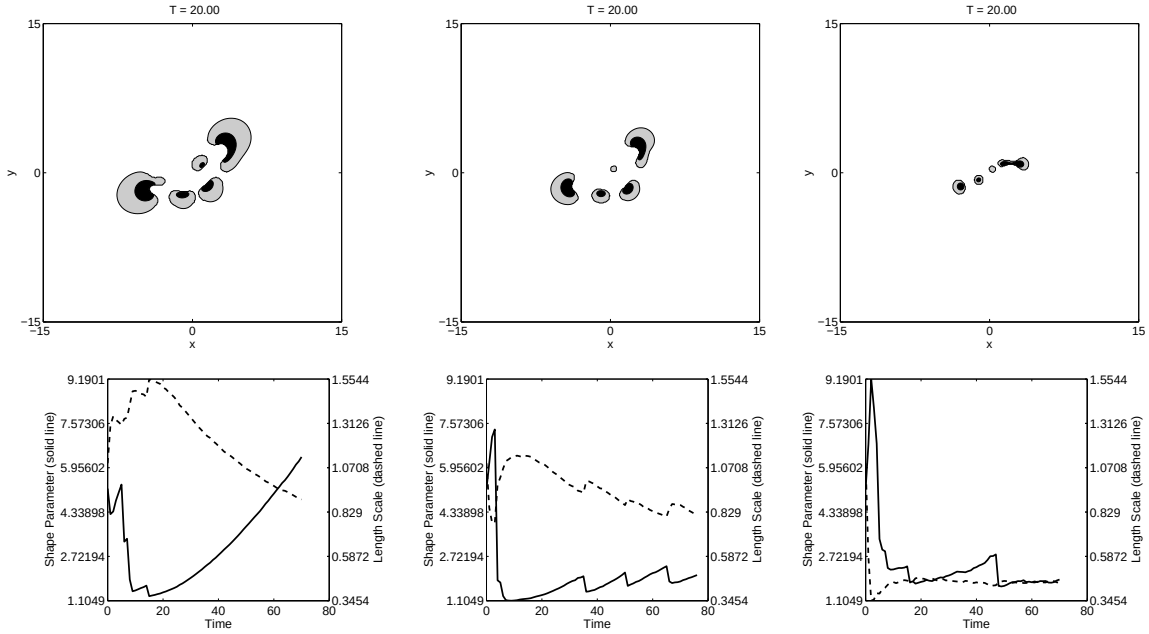

Fig. A.10. The effect of N on fragmenting tumor growth into nutrient-poor, low–mobility tissue ($D = 1$, $\mu = 1$): From left to right: $N = 0.175$, $N = 0.350$, and $N = 0.700$. The top row gives the morphology at $T = 20.0$, and the bottom row plots the shape parameter $\mathcal{S}$ (solid curves) and length scale $\mathcal{LS}$ (dashed curves). $G = 20$, $G_N = 1$, and $A = 0$ for all three simulations.

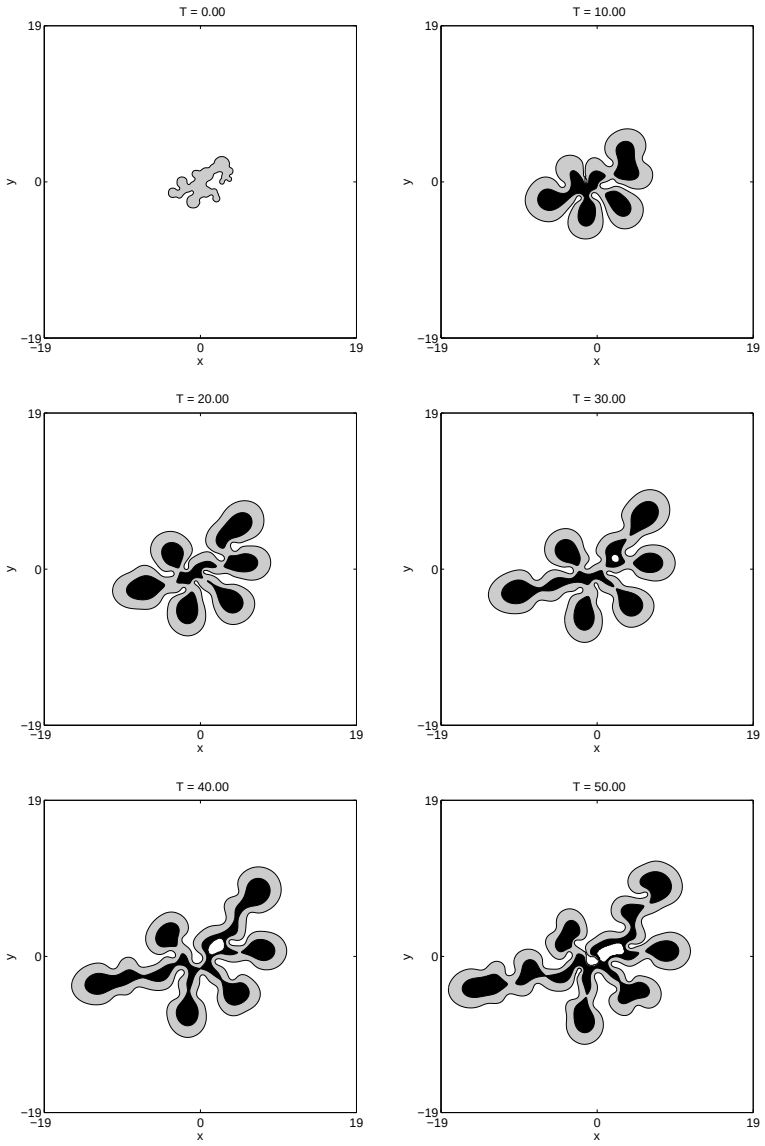

Fig. A.11. Long time simulation of invasive, fingering growth into nutrient-rich ($D = 50$), low-mobility ($\mu = 1$) tissue. Plots are in $T = 10.0$ increments, $G = 20$, $G_N = 1$, $N = 0.35$, and $A = 0$.

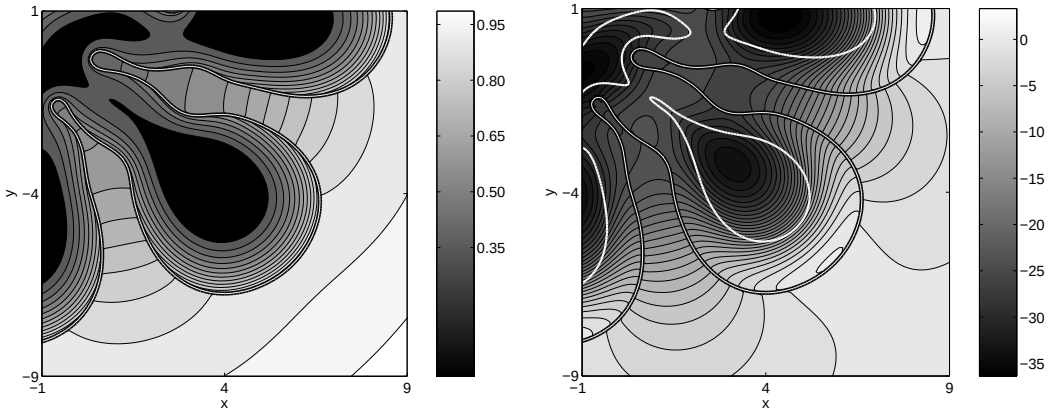

Fig. A.12. Contours of the nutrient concentration (left) and pressure (right) between growing fingers from the previous simulation at time $T = 20.0$. In the nutrient figure, the black region denotes where $\sigma < N$, and in the pressure figure, the boundary of the necrotic core is given by the white curve. Notice that the pressure gradient is primarily parallel to the fingers.

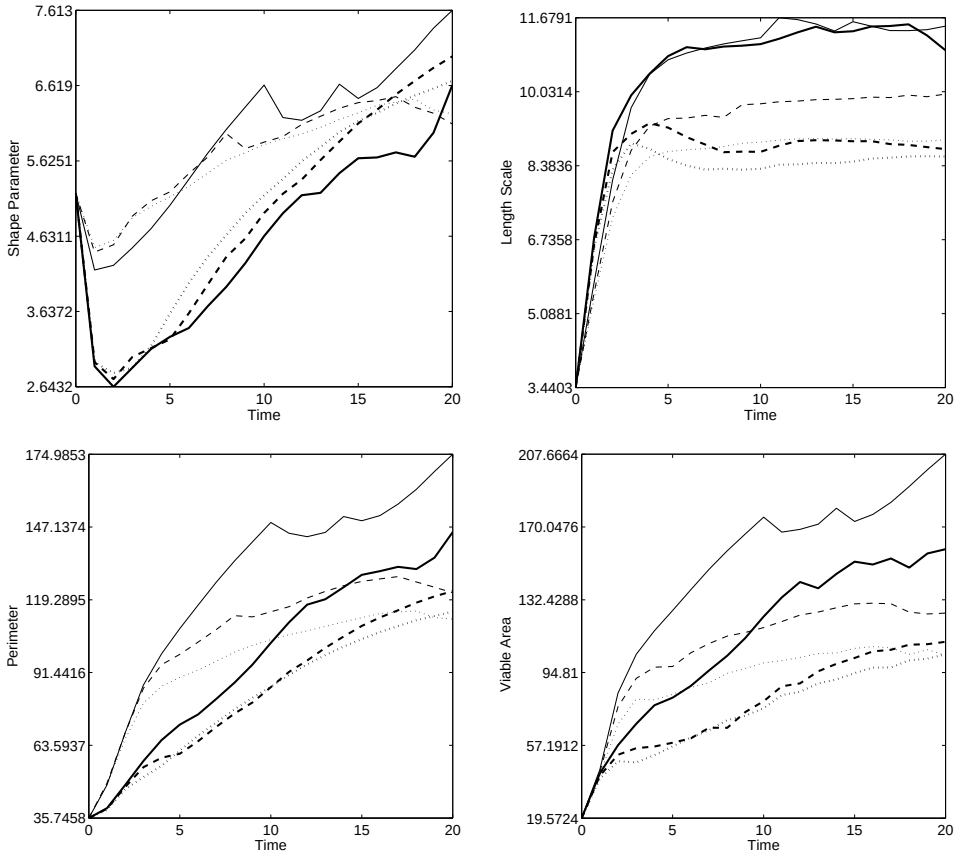

Fig. A.13. Evolution of the shape parameter $\mathcal{S}$ (top left), length scale $\mathcal{LS}$ (top right), perimeter (bottom left), and viable tumor area (bottom right) for invasive, fingering growth into nutrient-rich, low-mobility tissue (thin curves: $\mu = 0.25$, thick curves: $\mu = 1$). In all plots, dotted lines are for $D = 50$, dashed lines are $D = 100$, and solid lines are $D = \infty$.

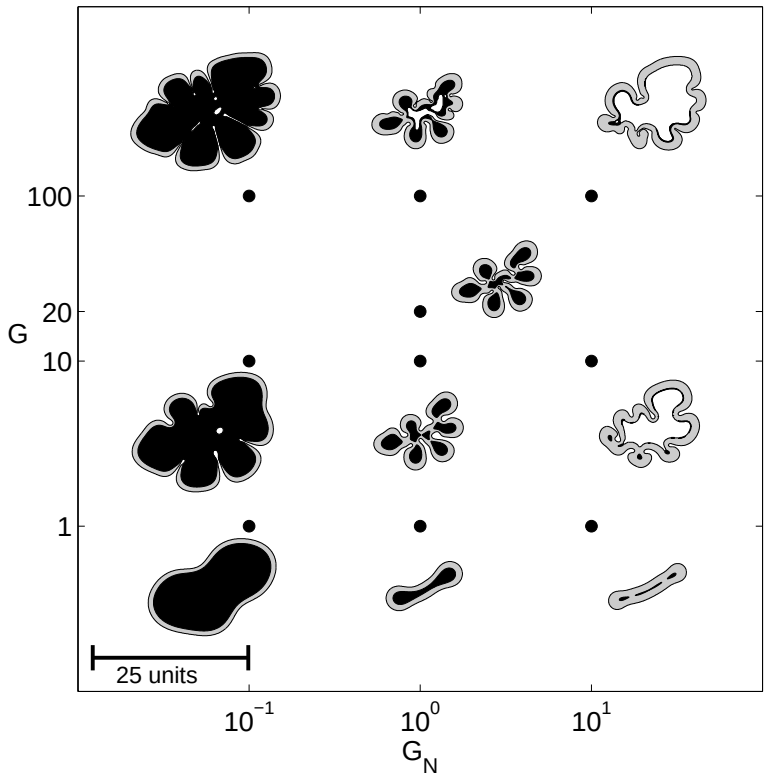

Fig. A.14. Parameter study in G and G_N for invasive, fingering tumor growth into nutrient-rich, low-mobility tissue ($D = 50$, $\mu = 1$). The tumor aggressiveness parameter G increases from bottom to top, and the necrotic degradation parameter G_N increases from left to right.

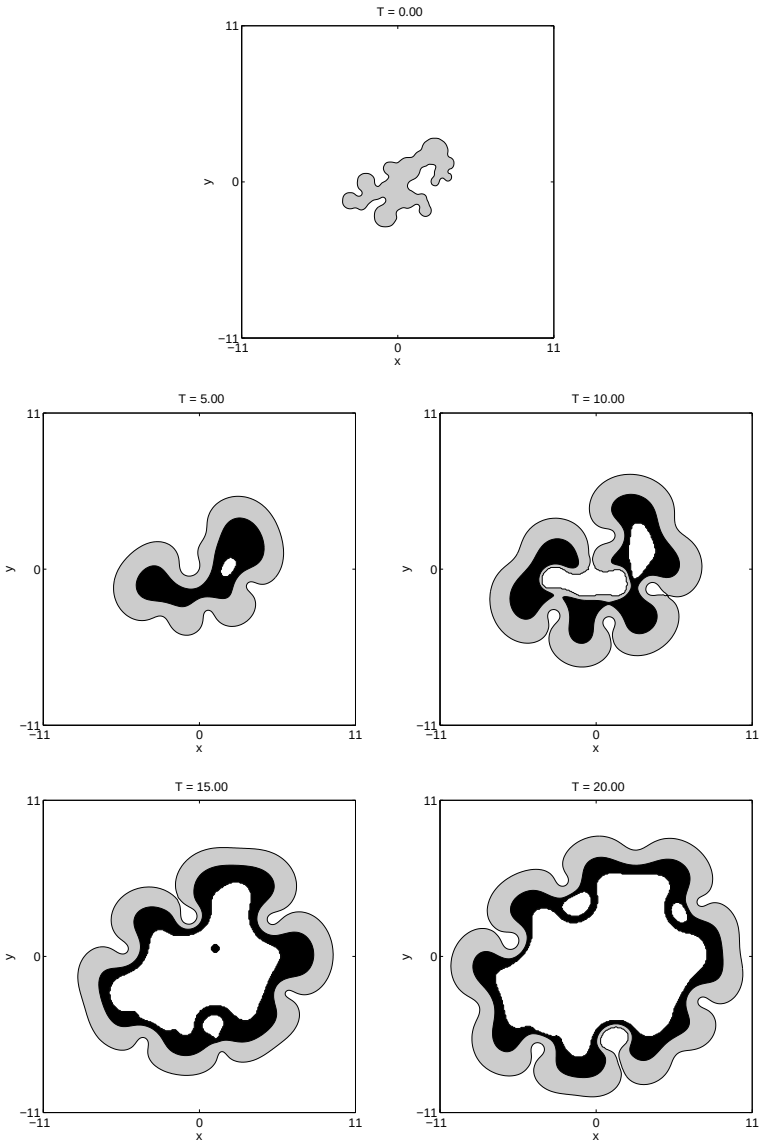

Fig. A.15. Long time simulation of compact tumor growth into nutrient-rich, high–mobility tissue ($D = 100$, $\mu = 50$). Plots are in $T = 10.0$ increments, with $G = 20$, $G_N = 1$, $N = 0.35$, and $A = 0.0$.

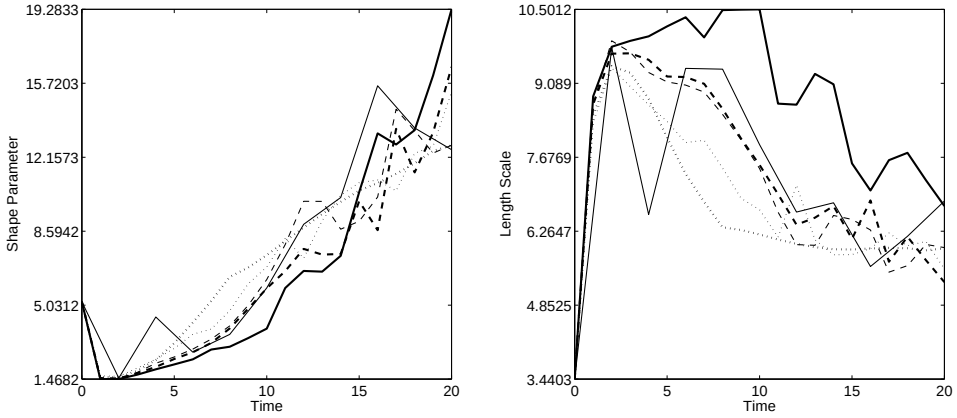

Fig. A.16. Evolution of the shape parameter $\mathcal{S}$ (left) and length scale $\mathcal{LS}$ (right) for compact growth into nutrient-rich, high-mobility tissue (thin curves: $\mu = 50$, thick curves: $\mu = \infty$). In all plots, dotted curves are for $D = 50$, dashed curves designate $D = 100$, and solid curves give $D = \infty$.

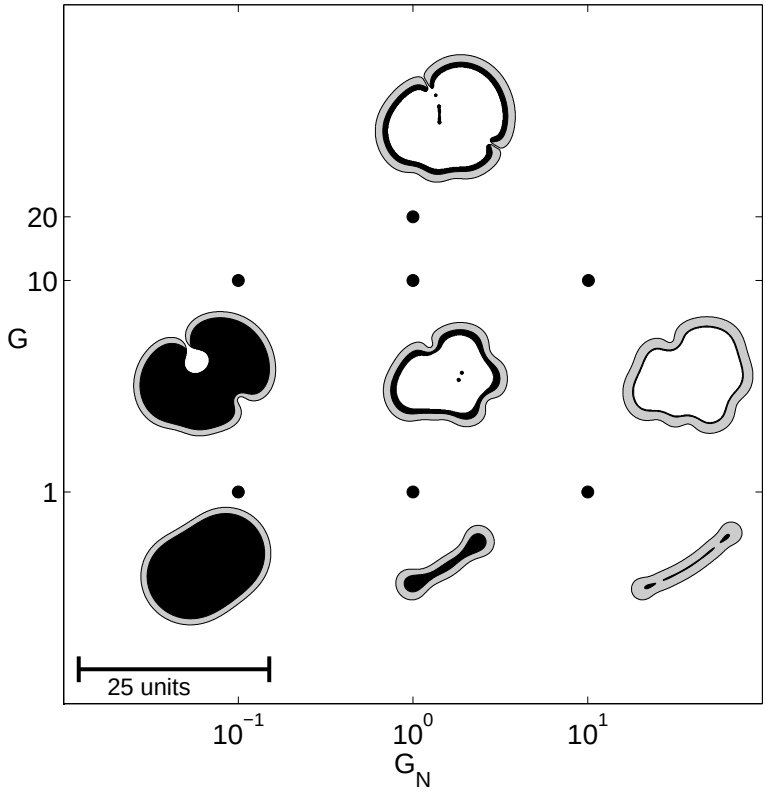

Fig. A.17. Parameter study in G and G_N for compact tumor growth into nutrient-rich, high-mobility tissue ($D = 50$, $\mu = \infty$). The tumor aggressiveness parameter G increases from bottom to top, and the necrotic degradation parameter G_N increases from left to right.

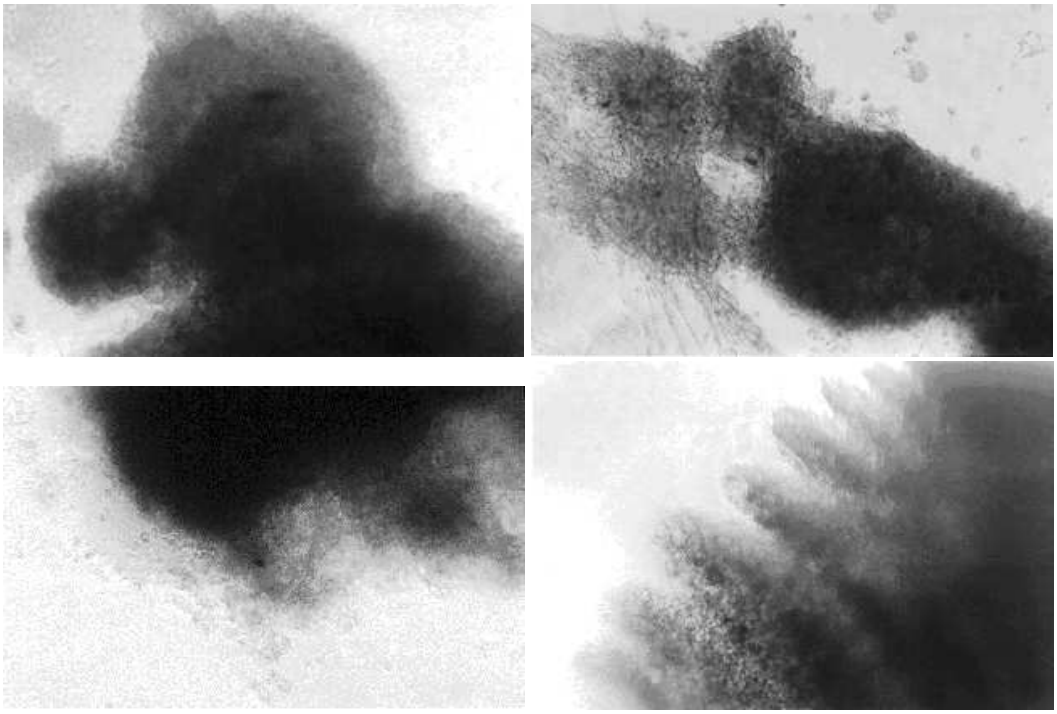

Fig. A.18. *in vitro* experimental evidence from the study by Frieboes et al. (2006b) of predicted tumor morphologies. **Lower left:** low glucose, 1% FBS. **Lower right:** high glucose, 1% FBS. **Upper left:** low glucose, 10% FBS. **Upper right:** high glucose, 10% FBS.

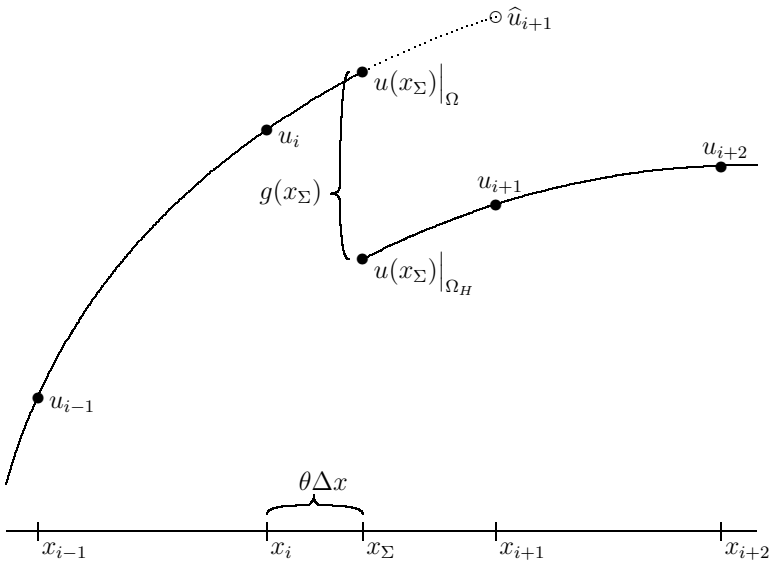

Fig. A.19. Discretizing $\alpha\nabla^2 u$ across the interface at x_Σ by a ghost fluid extension to $\widehat{u}_{i+1}$. Care must be taken to enforce the jump boundary conditions $[u] = g$ and $[\alpha\nabla u \cdot \mathbf{n}] = 0$.